Review

Self-Starting Soliton–Comb Regimes in $\chi^{(2)}$ Microresonators

Sergey Smirnov [1], **Evgeni Podivilov** [2] **and Boris Sturman** [2,*]

[1] Nonlinear Photonics Laboratory, Novosibirsk State University, 630090 Novosibirsk, Russia
[2] Institute of Automation and Electrometry, Russian Academy of Sciences, 630090 Novosibirsk, Russia
[*] Correspondence: sturman@iae.nsk.su

Abstract: The discovery of stable and broad frequency combs in monochromatically pumped high-Q optical Kerr microresonators caused by the generation of temporal solitons can be regarded as one of the major breakthroughs in nonlinear optics during the last two decades. The transfer of the soliton–comb concept to $\chi^{(2)}$ microresonators promises lowering of the pump power, new operation regimes, and entering of new spectral ranges; scientifically, it is a big challenge. Here we represent an overview of stable and accessible soliton–comb regimes in monochromatically pumped $\chi^{(2)}$ microresonators discovered during the last several years. The main stress is made on lithium niobate-based resonators. This overview pretends to be rather simple, complete, and comprehensive: it incorporates the main factors affecting the soliton–comb generation, such as the choice of the pumping scheme (pumping to the first or second harmonic), the choice of the phase matching scheme (natural or artificial), the effects of the temporal walk off and dispersion coefficients, and also the influence of frequency detunings and Q-factors. Most of the discovered nonlinear regimes are self-starting—they can be accessed from noise upon a not very abrupt increase in the pump power. The soliton–comb generation scenarios are not universal—they can be realized only under proper combinations of the above-mentioned factors. We indicate what kind of restrictions on the experimental conditions have to be imposed to obtain the soliton–comb generation.

Keywords: microresonator; frequency comb; soliton; phase matching; walk off; lithium niobate

1. Introduction

The generation of broad frequency combs, i.e., of long sequences of equidistant coherent light lines, in monochromatically pumped high-Q Kerr microresonators [1–5] can be regarded as one of the main discoveries in nonlinear optics during the last two decades. Remarkably, the spectral positions of these lines do not generally coincide with (or are not close to) the discrete resonator modes because of the dispersion of the latter. This is why the interpretation of the combs as a sequential parametric excitation of new resonator modes is rather fruitless. The right physical picture of the frequency comb in question is proven to be the generation of a spatially narrow soliton propagating along the resonator rim with a constant velocity v_0 [5]. Fourier expansion of the light field employing its periodicity over the circumference ensures the equidistance of the light lines with the frequency spacing v_0/R, where R is the major resonator radius. Thus, the comb and soliton are two physical terms expressing different properties of the same nonlinear light state. Most probably, the soliton nature of broad frequency combs has no alternative.

The soliton–comb concept is nowadays generally accepted for $\chi^{(3)}$ resonators. It is applicable not only to glass-based Kerr microresonators, but also to resonators made of $\chi^{(3)}$ crystals [5–10]. One can speak of the corresponding comb technology. The amount of publications on the $\chi^{(3)}$ combs can be estimated as $\sim 10^2$. Note that the dissipative solitons in question are essentially different from (and more complicated than) the so-called conservative solitons associated typically with the nonlinear Schrödinger equation [11,12]. The dissipative solitons balance not only the dispersion broadening and nonlinear compression but also the gain owing to external pumping and the resonator losses.

The transfer of the soliton–comb concept to the $\chi^{(2)}$ microresonators, which possess the lower second-order nonlinearity, promises further lowering of the pump power, entering of new spectral ranges, and new attractive operation regimes; see also below. This transfer cannot be straightforward because of the specific and important features inherent in the $\chi^{(2)}$ nonlinearity [13]. In contrast to the $\chi^{(3)}$ case, elementary nonlinear processes involve not four but three light quanta. These processes are the thresholdless generation of the second harmonic (or sum frequencies) and the inverse threshold process of parametric oscillation. The $\chi^{(2)}$ comb generation can be viewed as a cascade of these processes. Running them requires the employment of the phase matching (PM) for the first harmonic (FH) and second harmonic (SH) resonator modes. The PM conditions in the $\chi^{(2)}$ microresonators can in turn be either natural, relevant to certain light wavelengths, or artificial using the so-called radial poling [14–18]; see also below.

As soon as mutually coupled FH and SH modes are distinguished, we must deal with the *duality* of the $\chi^{(2)}$ solitons and combs—each of them must consist of FH and SH components; see also Figure 1. The presence of subcombs in the FH and SH frequency domains can definitely be regarded as a positive feature. Additionally, two different pumping schemes (pumping into FH or SH resonator modes) have to be envisaged. These FH and SH pumping cases are substantially different. The presence of the temporal walk off between the FH and SH modes, which can be viewed as the difference in the corresponding group velocities, is also an important feature of the $\chi^{(2)}$ case. The effect of the walk off on the soliton–comb generation is generally negative—it has to be minimized when possible. Furthermore, the presence of two dispersion coefficients, relevant to the FH and SH spectral ranges, has to be taken into account. Generally, the $\chi^{(2)}$ case provides much more room for the search for soliton–comb regimes as compared to the $\chi^{(3)}$ case. Conservative solitons in $\chi^{(2)}$ media, which can be regarded as the basis for dissipative cavity solitons, are reviewed in [19].
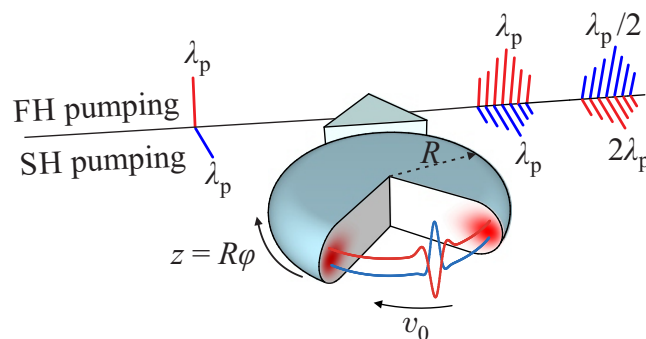

Figure 1. Schematic of $\chi^{(2)}$ comb generation; R and φ are the major resonator radius and the azimuth angle. The output comb spectra are due to a dual FH-SH soliton propagating along the resonator rim with velocity v_0. The red spots indicate localization of the resonator modes near the rim.

Axially symmetric $\chi^{(2)}$ microresonators are widespread [17,18,20–23]. Their linear properties are largely common with those of the $\chi^{(3)}$ resonators [17,24–26]. Each resonator can be characterized by a major radius R, see Figure 1. The modes (whispering gallery modes) are localized near the resonator rim, and the rim shapes can be different. Each mode can be labeled by an integer azimuth number m and, additionally, by two transverse modal numbers. All modal functions are proportional to $\exp(im\varphi)$, where φ is the azimuth angle. While exact analytical solutions exist only for spherical resonators, approximate methods to calculate the modal frequencies, functions, and nonlinear interactions are well developed [24,27–31]. This is also relevant to the methods for coupling light into and out of the resonator. Owing to the presence of a coupler (tapered fiber, prism, etc.), the inverse total (loaded) quality factor Q^{-1} consists of internal and coupling contributions.

The most common lithium niobate (LN) based $\chi^{(2)}$ resonators are discs with the major radius $R \sim 1$ mm, the minor radius $r \lesssim R$, and quality factors $Q = (10^7$–$10^8)$ [17,18]. The

resonator modes can be viewed as quasiplane waves with frequencies $\omega \equiv 2\pi c/\lambda = k_m c/n$, discrete wavenumbers $k_m = m/R$, and an effective refractive index n depending on the modal numbers, R, and r. For $R > 1$ mm, n is close to the bulk index $n_b(\lambda)$; the difference $n - n_b$ characterizes the effects of the geometric dispersion. In the optical range, the azimuth number $m = 2\pi n R/\lambda$ is $\sim 10^4$. The frequency distance $\delta\omega = c/nR$ between neighboring modes with $\delta m = 1$ is much larger than the line width. As LN is a uniaxial optical material, modes with ordinary (o) and extraordinary (e) polarizations have to be distinguished. In addition to lithium niobate, other polar crystals such as lithium tantalate, beta-lithiun borate, and aluminium nitride can be used to manufacture high-quality, $Q \approx (10^6$–$10^8)$, microresonators for the visible and UV spectral ranges [18,32,33].

Investigations of the SH generation and parametric oscillation in $\chi^{(2)}$ microresonators are also known [17,18]. In LN resonators, the PM condition for the SH generation, $\omega_{2m} = 2\omega_m$, can be fulfilled naturally at the FH wavelength $\lambda_1 \simeq 1064$ nm with the use of o- and e-polarized FH and SH modes [14]. The parametric oscillation for this natural (birefringent) PM corresponds to the SH wavelength $\lambda_2 = \lambda_1/2 \simeq 532$ nm. Here and later, the subscripts 1 and 2 refer to the FH and SH ranges, respectively. The employment of the radial poling in LN resonators [15–18] enables one to fulfill the quasi-PM conditions at practically any wavelength on demand via a controllable breaking of the axial symmetry. It is also necessary to mention that, because of very small resonator line widths, fine tuning means (such as the temperature or geometric tuning) have to be used to control the linear and nonlinear phenomena [17,18,25,34].

Both the $\chi^{(3)}$ and $\chi^{(2)}$ combs originate from parametric instabilities inside the resonators. This is why the continuous-wave monochromatic pump is able to generate temporal solitons. The threshold pump power for the instability $\mathcal{P}$th is largely controlled by the relevant modal Q factors. Roughly speaking, in the $\chi^{(3)}$ and $\chi^{(2)}$ cases, $\mathcal{P}$th is proportional to Q^{-2} and Q^{-3}, respectively. For $Q \gtrsim 10^7$, the $\chi^{(2)}$ nonlinearity is typically dominating, and $\mathcal{P}$th belongs to the μW range [17,18].

Initial experimental and theoretical attempts to obtain $\chi^{(2)}$ combs dealt with bulk systems [35–41] that are quite specific in physics and relevant to much higher threshold pump powers. While some tens of comb lines were observed, neither solitons nor broad comb spectra were reported. Recently, the first experimental efforts to generate the $\chi^{(2)}$ combs in microresonators have been made [42–45]. No soliton–comb regimes have been observed so far to the best of our knowledge. Furthermore, we can claim that this failure is in agreement with our theoretical results on the necessary conditions for the realization of such regimes. Therefore, we see the main tasks of this mini-review in (i) the determination of the conditions for the $\chi^{(2)}$ soliton–comb generation and (ii) in the predictions of the main properties of the soliton–comb states. Additionally, we will indicate where and why the necessary conditions were violated in the known experiments. Lastly, we will compare our findings with the known early predictions for the $\chi^{(2)}$ soliton–comb states [46–49]. As far as possible, the cases considered will be applied to experimentally realizable and important situations.

A considerable part of the literature on nonlinear phenomena in microresonators, see, e.g., [4,17,20,44], extensively employs the quantum–mechanical terminology and notation deeply within the classical domain, where the applicability of the classical Maxwell equations is beyond any doubt. Being well developed and attracting, the quantum–mechanical formalism here is out of place and confusing. We claim that it can easily be replaced by the classical Hamiltonian formalism [50,51]. Keeping all merits of the quantum formalism, it is fully adequate to the situation.

2. Basic Equations, Parameters, and Definitions

2.1. Periodic and Antiperiodic States

First, let the pump frequency ω_p be close to a modal frequency and the FH-SH phase matching be natural, i.e., the azimuth symmetry takes place. Then, two variants have to be considered, namely pumping into a FH and into a SH mode. In the FH pumping

case, the PM condition $\omega(2m_1^0) \simeq 2\omega(m_1^0)$ can be satisfied with a high accuracy only for a single azimuth number m_1^0. It is implied that the frequency detunings $\omega_p - \omega(m_1^0)$ and $\omega(2m_1^0) - 2\omega(m_1^0)$ are much smaller in the values than the intermodal distance c/nR. The light electric field $E(\varphi, t)$ can be represented as

$$E = E_1\, e^{\mathrm{i}(m_1^0\varphi - \omega_p t)} + E_2\, e^{2\mathrm{i}(m_1^0\varphi - \omega_p t)} + c.c., \tag{1}$$

where $E_1(\varphi, t)$ and $E_2(\varphi, t)$ are slowly varying (and generally vectorial) FH and SH amplitudes (envelopes). Obviously, these amplitudes are 2π-periodic in φ, and the SH azimuth number $m_2^0 = 2m_1^0$ is even.

In the SH pumping case, the situation is different, as illustrated by Figure 2. The above PM condition can be fulfilled only if the azimuth number of the pumped mode m_2^0 is even (Figure 2a). If m_2^0 is odd (Figure 2b), two FH modes (with even and odd azimuth numbers) must be excited. Here, the simplest PM conditions are $\omega_{m_2^0} = \omega_{m_1^0} + \omega_{m_1^0+1}$, $m_2^0 = 2m_1^0 + 1$. Let us use (regardless of the parity of m_2^0) the ansatz

$$E = E_1\, e^{\mathrm{i}(m_2^0\varphi - \omega_p t)/2} + E_2\, e^{\mathrm{i}(m_2^0\varphi - \omega_p t)} + c.c. \tag{2}$$

for the light field. Then, the first exponential factor is 2π periodic for an even m_2^0 and 2π antiperiodic for an odd m_2^0. As the true light field $E(\varphi, t)$ is 2π periodic, we must accept that the FH amplitude $E_1(\varphi, t)$ is antiperiodic for the odd m_2^0; i.e., $E_1(\varphi, t) = -E_1(\varphi \pm 2\pi, t)$. The SH amplitude is still 2π periodic, $E_2(\varphi, t) = E_2(\varphi \pm 2\pi, t)$. A dual FH-SH state with an antiperiodic amplitude E_1 and periodic amplitude E_2 is named the antiperiodic state [52,53]. The antiperiodic sates (solutions) are topologically different from the conventional periodic states. No temporal evolution can make the conversion between these two states. To the best of our knowledge, the separation of the light states into periodic and antiperiodic ones is original, and it was never implemented for bulk $\chi^{(2)}$ systems. We stress that the antiperiodic states are relevant to pumping into an odd SH mode. Otherwise, we have a periodic dual state, such that $E_1(\varphi, t) = E_1(\varphi \pm 2\pi, t)$ and $E_2(\varphi, t) = E_2(\varphi \pm 2\pi, t)$.
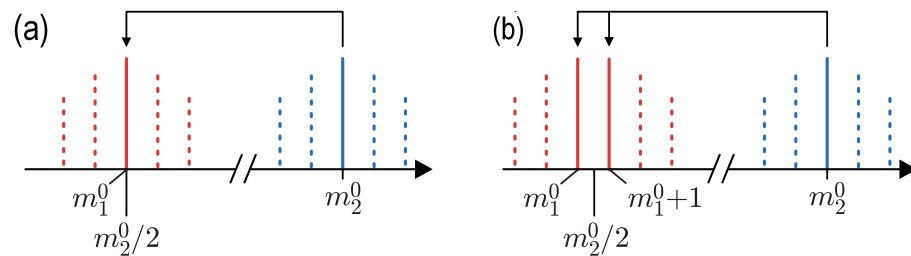

Figure 2. The excitation of periodic (**a**) and antiperiodic (**b**) states for SH pumping into even and odd resonator modes. The primary FH azimuth number $m_1^0 = m_2^0/2$ is an integer in (**a**) and semi-integer in (**b**). Side harmonics arise automatically in (**b**) above the threshold.

Using the above vectorial notation, we wanted to stress the generality of the periodic and antiperiodic light states for the $\chi^{(2)}$ nonlinearity. While the FH and SH resonator modes can be different in polarization, one can always deal with scalar FH and SH amplitudes denoted in what follows as F and S.

2.2. Equations for the Modal Amplitudes

Now, we write down nonlinear equations for the complex modal amplitudes F_{m_1} and S_{m_2} relevant to the FH and SH frequency domains. It is assumed, as in all known theoretical studies, that the modal polarization and the transverse modal numbers stay the same within each of these domains. We start from the phase matching case relevant to an even azimuth number $m_2^0 = 2m_1^0$ in the absence of radial poling (full azimuth symmetry). This takes place for the FH pumping and is also applicable to the SH pumping into an even mode, see Figure 2a. It is useful to count the FH and SH frequencies from ω_1 and ω_2. In

accordance with Equations (1) and (2), $\omega_1 = \omega_p$, $\omega_2 = 2\omega_p$ in the FH pumping case, while $\omega_1 = \omega_p/2$, $\omega_2 = \omega_p$ in the case of SH pumping. Furthermore, instead of m_1 and m_2, we introduce the more convenient FH and SH modal numbers $j = m_1 - m_1^0 = 0, \pm 1, \ldots$ and $l = m_2 - m_2^0 = 0, \pm 1, \ldots$. With these preliminaries, we have

$$i\dot{F}_j - Z_{1,j}F_j = 2\mu \sum_l S_l F_{l-j}^* + ih_1\delta_{j0}$$

$$i\dot{S}_l - Z_{2,l}S_l = \mu \sum_j F_j F_{l-j} + ih_2\delta_{l0} \,. \tag{3}$$

Here, the dots indicate the differentiation in time; $Z_{1,j} = \omega_j - \omega_1 - i\gamma_j$ and $Z_{2,l} = \omega_l - \omega_2 - i\gamma_l$, $\gamma_{j,l} = \omega_{j,l}/2Q_{j,l}$ are the modal decay rates; μ and $h_{1,2}$ are the nonlinear coupling coefficient and the internal pump amplitudes, respectively; and $\delta_{j0,l0}$ are the Kronecker deltas. For the FH and SH pumping, we have $h_2 = 0$ and $h_1 = 0$, respectively. The modal amplitudes F_j and S_l are defined such that $\omega_j|F_j|^2$ and $\omega_l|S_l|^2$ are the modal energies. This definition corresponds to the classical Hamiltonian formalism [50]. The dimensionless quantities $|F_j|^2/\hbar \gg 1$ and $|S_l|^2/\hbar \gg 1$ are nothing but the number of modal FH and SH light quanta in the classical limit. The presence of a factor of 2 in set (3) reflects the Hamiltonian nature of the nonlinear interaction—the total energy is conserved for $h_{1,2} = 0$ and $\gamma_{j,l} = 0$.

The coefficients μ and $h_{1,2}$ can be determined in a quite general manner via modeling the modes and their coupling in and out of the resonator [29,31]:

$$\mu \simeq \frac{d\omega_p^{3/2}}{2n^3 R^{1/2}\sigma_{\text{eff}}^{1/2}}, \quad h_{1,2} \simeq \left(\frac{\mathcal{P}_0}{\tilde{Q}_{1,2}}\right)^{1/2}, \tag{4}$$

where d is the relevant component of the conventional susceptibility tensor, σ_{eff} is the effective interaction cross-section, $\mathcal{P}_0$ is the pump power, $\tilde{Q}^{-1}$ is the coupling contribution to Q^{-1}, and $n \simeq n_{\text{o}} \simeq n_{\text{e}}$ is a representative refraction index. Further details can be found in Section S1 of the Supplementary Materials.

The rate coefficients $Z_{1,j}$ and $Z_{2,l}$ can be expressed by the group velocities $v_{1,2}$ and dispersion coefficients $v'_{1,2}$ if we use the expansion $\omega(k) = \omega(k_0) + v\delta k + v'\delta k^2/2$ with $\delta k = k - k_0$ near the points $k_0 = m_1^0/R$ and m_2^0/R:

$$Z_{1,j} = \Delta_1 - i\gamma_1 + v_1 j/R + v'_1 j^2/2R^2 \tag{5}$$

$$Z_{2,l} = \Delta_2 - i\gamma_2 + v_2 j/R + v'_2 l^2/2R^2.$$

The parameters v and v' are expressed by the refractive index $n(\lambda)$: $v = c/(n - \lambda n')$ and $v' = -c\lambda^3 n''/2\pi(n - \lambda n')^2$, where the prime indicates the differentiation in λ. Knowledge of the dependences $n_{\text{o,e}}(\lambda)$, with or without the geometric dispersion, enables one to calculate $v_{1,2}$ and $v'_{1,2}$ as functions of λ_2 and $\lambda_1 = 2\lambda_2$. Further details can be found in Section S2 of the Supplementary Materials. Expressions for detunings $\Delta_{1,2}$ depend on the pumping scheme. For the FH pumping, $\Delta_1 = \omega_{m_1^0} - \omega_p$ and $\Delta_2 = \omega_{m_2^0} - 2\omega_p$. In the SH pumping case, $\Delta_2 = \omega_{m_2^0} - \omega_p$ and $\Delta_1 = (2\omega_{m_1^0} - \omega_p)/2$.

Consider now the remaining case of SH pumping into a mode with an odd azimuth number m_2^0 when two FH modes with even and odd azimuth numbers enter the phase matching condition, see also Figure 2b. The SH modes can be numerated again with the integer $l = m_2 - m_2^0 = 0, \pm 1, \ldots$. The only way to symmetrically numerate the FH modes is to introduce a semi-integer number $j = \pm 1/2, \pm 3/2, \ldots$ such that $m_1 = m_2^0/2 + j$. The form of sets (3) and (5) remains the same, and the only difference is in the expression for detuning Δ_1: $\Delta_1 = (\omega_{m_1^0} + \omega_{m_1^0+1} - \omega_p)/2$.

2.3. The Impact of Radial Poling

The radial poling enables one to adjust the phase matching to practically any desirable spectral point with no effect on the linear properties. In polar $\chi^{(2)}$ materials, such as LN, the largest components of the quadratic susceptibility tensor, d_{13} and d_{33}, change sign under the inversion of the spontaneous polarization. The periodic radial poling results in the φ periodic sign changing for any of these components, as illustrated schematically by Figure 3a. Let d have the absolute value d_0. The periodic sign-changing function $d(\varphi)$ can be represented then by the Fourier series

$$d = \sum_s d_s \exp(\mathrm{i}s\varphi) \, . \tag{6}$$

If $\mathcal{N}$ is the number of poling periods, the nonzero components d_s correspond to $s = 0, \pm\mathcal{N}, \pm 2\mathcal{N}, \ldots$. In the case of the $\pm$ symmetric radial domain structure (50% duty cycle ratio), which is the most suitable for quasiphase matching, only the Fourier harmonics with odd ratios $s/\mathcal{N} = \pm 1, \pm 3, \ldots$ are nonzero. For these harmonics $|d_s| = 2d_0\mathcal{N}/\pi|s|$, see also Figure 3b. The reduction factor $|d_s|/d_0$ decreases with an increasing $|s|/\mathcal{N}$ but remains comparable with 1 for $|s| = \mathcal{N}$. Typically $\mathcal{N} \gg 1$, and the neighboring peaks are well separated from each other.
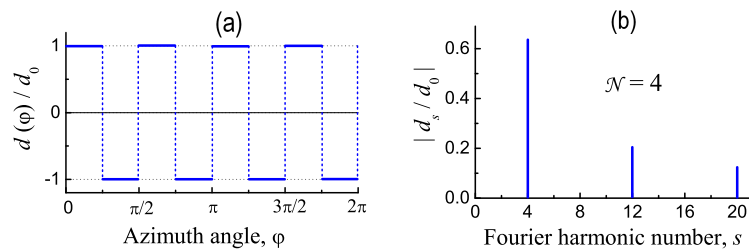

Figure 3. (**a**) Illustration of the azimuth dependence of the susceptibility coefficient $d(\varphi)$ for a perfect symmetric radial domain pattern with $\mathcal{N} = 4$. (**b**) First three harmonics of the corresponding Fourier spectrum with $s = \mathcal{N}, 3\mathcal{N}$, and $5\mathcal{N}$.

The employment of the largest first Fourier harmonics of $d(\varphi)$ for quasiphase matching corresponds to the PM condition $2\omega_{m_1^0} = \omega_{2m_1^0 \pm \mathcal{N}}$ for SH generation. The sign "plus" is relevant to the most typical case of decreasing wavelength dependence of the refraction index $n(\lambda)$ [32]. We see that the SH azimuth number $m_2^0 = 2m_1^0 \pm \mathcal{N}$ is even for an even alternation number $\mathcal{N}$ and odd for an odd number $\mathcal{N}$. In the second case, SH pumping leads to the excitation of periodic states. In the case of the odd combination $m_2^0 \mp \mathcal{N}$, the above PM condition cannot be fulfilled. However, we can fulfill the PM condition $\omega_{m_1^0} + \omega_{m_1^0+1} = \omega_{2m_1^0 \pm \mathcal{N}}$, which leads to the excitation of the antiperiodic states. Thus, the quasi-PM by means of the radial poling results in a controllable shift of the FH azimuth number m_1^0. The set (3) for the FH and SH amplitudes results in them staying unchanged.

Note that microresonators made of commercial PPLN wafers [20] are not appropriate for the spectral adjustment in question. The spectrum $|d_s|$ includes in this case many significant peaks $|d_{\mathcal{N}\pm 1}|, |d_{\mathcal{N}\pm 2}|, \ldots$ in addition to $|d_{\mathcal{N}}|$, which leads to unwanted interference of many cascading $\chi^{(2)}$ processes.

The possibility to adjust the phase matching to any spectral range raises the question about the specific goals and properties of the radial poling. Figure 4 shows the dependences $v_{1,2}(\lambda)$ and $v'_{1,2}(\lambda)$ for the e-polarized modes in a LN-based resonator with $R = 1.5$ mm. The effects of geometric dispersion are very weak here. The zero walk-off point corresponds to $\lambda_2^c \simeq 1349$ nm, where the dispersion coefficients v'_1 and v'_2 are opposite in signs. The vicinity of this point, as will be shown below, is especially attractive for the soliton–comb generation. The number of periods $\mathcal{N}$ necessary to achieve quasi-PM at this point can be estimated as 284. Further details can be found in Section S3 of the Supplementary Materials.
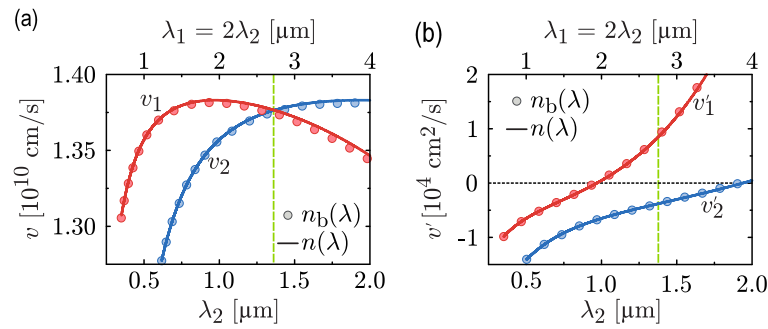
(a)

$\lambda_1 = 2\lambda_2$ [μm]

(b)

$\lambda_1 = 2\lambda_2$ [μm]

Figure 4. Dependences $v_{1,2}(\lambda)$ (**a**) and $v'_{1,2}(\lambda)$ (**b**) for a LN-based resonator with $R = 1.5$ mm and $R/r = 3$. The dotted and solid lines refer to the bulk index n_b and the effective index n incorporating the effects of geometric dispersion. The vertical line $\lambda_2 = \lambda_2^c \simeq 1.349$ μm ($\lambda_1 = \lambda_1^c \simeq 2.698$ μm) corresponds to zero walk-off point $v_1 = v_2$.

2.4. Fundamental z, t Representation

The primary set (3) of the ordinary differential equations is convenient for numerical simulations. However, many fundamental features of the soliton–comb states become more evident if we transform it to a set of partial differential equations. This can be performed in terms of the FH and SH amplitudes $F(\varphi, t)$ and $S(\varphi, t)$ defined by the Fourier expansions

$$F = \sum_j F_j \exp(ij\varphi), \quad S = \sum_l S_l \exp(il\varphi). \tag{7}$$

For integer values of j, l, this leads automatically to the periodic states, while for integer l and semi-integer j, we arrive at an antiperiodic state.

Using Equations (3), (5) and (7) and introducing the rim coordinate $z = R\varphi$, one can make sure that the periodic and antiperiodic states obey the same set of nonlinear equations for any phase-matching scheme [52,53]:

$$\begin{aligned}
[\ i(\partial_t + v_1\partial_z) + (1/2)\,v'_1\partial_z^2 - \Omega_1]F &= 2\mu SF^* + ih_1 \\
[\ i(\partial_t + v_2\partial_z) + (1/2)\,v'_2\partial_z^2 - \Omega_2]S &= \mu F^2 + ih_2 \,,
\end{aligned} \tag{8}$$

where $\Omega_{1,2} = \Delta_{1,2} - i\gamma_{1,2}$. At perfect resonant pumping and phase matching, we have $\Delta_{1,2} = 0$. All parameters entering set (8) are known or controllable in experiment. For the $\chi^{(2)}$ solitons, set (8) plays a role that is similar to the role of the nonlinear Lugiato–Lefever equation for the $\chi^{(3)}$ soliton–comb states [4,5]. However, these two cases are fundamentally different. For the periodic states, equations analogous to set (8) can be found in [46–48].

Consider some important properties and useful transformations of set (8):

– This nonlinear set admits dual steady-state solutions $F(z - v_0 t)$, $S(z - v_0 t)$ circulating with a common velocity v_0 without shape changes. Solitons belong to this class of solutions. Velocity v_0 has to be determined simultaneously with the shape of the envelopes.

– Set (8) is written for a static coordinate frame. It is practical to rewrite it for a coordinate frame moving with velocity v_1. To conduct this, it is sufficient to drop the term $v_1\partial_z$ in the first equation and replace v_2 by $-v_{12} = v_2 - v_1$ in the second one. This is assumed from now on.

– In a dual steady state propagating with a constant velocity v_0, the modal amplitudes F_j and S_l oscillate in time as $\exp(-ijv_0 t/R)$ and $\exp(-ilv_0 t/R)$. This elementary property is useful to control the establishment of dual steady states in numerical simulations; see Section 4.

– Attempts to rewrite set (8) for the antiperiodic states using the replacements $F(z, t) = \tilde{F}(z, t)\exp(\pm iz/2R)$ lead to restoration of the periodicity but also to an explicit z-dependence of the right-hand sides (nonautonomous system). This is inappropriate.

The structure of Equation (8) gives a hint about the normalization of parameters relevant to the linear properties of the system. Such a normalization enables one to decrease the number of variable parameters. In what follows, we will use the following normalized detunings, walk off, and dispersion parameters $\delta_{1,2}$, α, and $\beta_{1,2}$:

$$\delta_{1,2} = \frac{\Delta_{1,2}}{\gamma_{1,2}}, \qquad \alpha = \frac{v_{12}}{\gamma_2 R}, \qquad \beta_{1,2} = \frac{v'_{1,2}}{2\gamma_{1,2}R^2}. \qquad (9)$$

As a rule, the actual values of the detunings are restricted by the inequalities $|\delta_{1,2}| \lesssim 1$. The actual values of α and $\beta_{1,2}$ substantially depend on the group velocity difference $v_{12} = v_1 - v_2$, the dispersion coefficients $v'_{1,2}$, and the decay rates $\gamma_{1,2}$.

For LN resonators, typical values of the decay rates are $\sim 10^7$, such that $|\beta_{1,2}| \ll 1$. On the contrary, we typically have $|\alpha| \gg 1$. Exceptions to this rule are possible near the zero walk-off point $\lambda_2 \simeq 1349$ nm. The decay rates γ_1 and γ_2 are typically not strongly different, such that the assumption $\gamma_{1,2} = \gamma$ can be used sometimes to simplify the modeling.

Generally speaking, the values of F, S, and $h_{1,2}$ also need some normalization. It is, however, different in the FH and SH pumping cases. We will provide the relevant information when necessary.

One more important property of set (8) is the presence of spatially uniform steady-state background solutions $\bar{F} \neq 0$, $\bar{S} \neq 0$ [54]. In the steady state, $F_0 = \bar{F}$ and $S_0 = \bar{S}$. Obviously, such a dual background is possible only for the periodic states. The dual background is closely related both to the properties of the solitons and to the thresholds of the instabilities leading to soliton–comb formation. Omitting all derivatives in (8), one can easily come to a closed algebraic equation for $|\bar{F}|^2$ that is, however, different for the FH and SH pumping cases. We have $|\bar{S}| = \mu|\bar{F}|^2/|\Omega_2|$ and $|\Omega_1|/2\mu$ for the FH and SH pumping cases, respectively. The dependence of $|\bar{F}|^2$ on the pump amplitudes $h_{1,2}$ is presented graphically in Figure 5. In both pumping cases, the dependence of $|\bar{F}|^2(h_{1,2})$ is controlled by the phase $\Phi = \arg(\Omega_1\Omega_2)$, such that multivalued solutions exist for sufficiently small $|\Phi|$. These dependences can be interpreted in the terms of the bifurcation theory [55]. This theory cannot, however, provide useful insights into the properties of light states well above the instability thresholds because of a very large number of the FH and SH light harmonics.
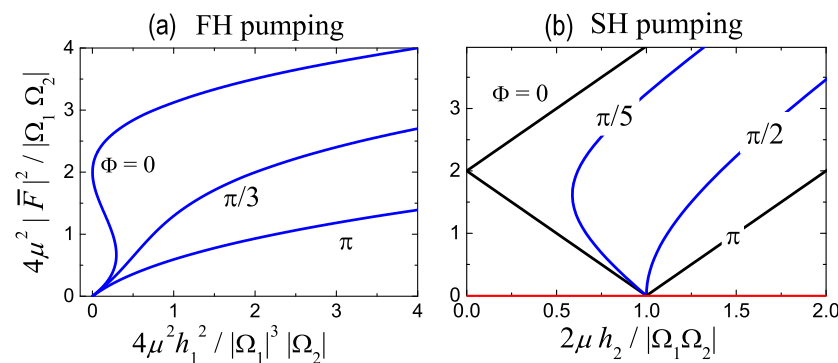

Figure 5. The normalized dependences of $|\bar{F}|^2$ on the pump strength parameters $h_{1,2}$ for the cases of FH (**a**) and SH (**b**) pumping. The curves are relevant to different values of the phase $\Phi = \arg(\Omega_1\Omega_2)$. Zero detuning case, $\Delta_{1,2} = 0$, corresponds to $\Phi = \pi$. The horizontal red line in (**b**) is related to the single background state $\bar{F} = 0$, $\bar{S} = -ih_2/\Omega_2$.

Importantly, the dual background with $\bar{F}, \bar{S} \neq 0$ always exists in the FH pumping case, see Figure 5a. At the SH pumping, the situation is different. For sufficiently small values of h_2, there is a single background state, such that $\bar{F} = 0$ and $|\bar{S}| = h_2/|\Omega_2| \neq 0$, see Figure 5b. This difference has dramatic consequences for the dual comb–soliton states, see Sections 4–6. Note also that Figure 5 gives a clear hint about the normalization of the amplitudes F, S and the pump amplitudes $h_{1,2}$ in the FH and SH pumping cases.

Lastly, we mention two limiting cases for set (8):

- In the limit $h_{1,2} \to 0$, $\gamma_{1,2} \to 0$ (no gain, no modal decay), we proceed to the conservative case reviewed in [19]. A number of exact soliton solutions are known here, but they are far from the subject of our study.
- In the dissipativeless driven limit $\gamma_{1,2} \to 0$ at $\Delta_{1,2} \neq 0$ and $h_{1,2} \neq 0$, one can also obtain exact soliton solutions [56]. It turns out, however, that they are all unstable, i.e., they cannot be realized.

3. Instability Thresholds

As is well known, the generation of second harmonic is thresholdless—it corresponds just to forced oscillation caused by the $\chi^{(2)}$ nonlinearity. This thresholdless process becomes merely more efficient in the presence of FH-SH phase matching. On the contrary, the excitation of FH harmonics in the presence of SH modes is always a coherent threshold process. This explains a big difference in the properties of the parametric excitation for the FH and SH pumping schemes in the microresonators [54].

The simplest and most efficient scheme is the SH pumping scheme. At sufficiently small pump powers (small values of h_2 at $h_1 = 0$), we deal simply with the linear excitation of the pumped mode m_2^0. Its steady-state amplitude is $S_0 = \bar{S} = h_2/(\gamma_2 + i\Delta_2)$, and detuning Δ_2 characterizes just the distance to the linear resonance. To see the effect of S_0 on the FH harmonics, we consider the first of Equation (3) with $S_l = S_0\delta_{l,0}$ and $h_1 = 0$. The quantities F_j and F_{-j}^* with an arbitrary j obviously obey two linear differential equations. Can they have a nonzero steady-state solution? Using the zero determinant solvability condition for linear algebraic equations and Equation (9) for the normalized parameters, we obtain the threshold condition in the form [52–54]

$$\eta_{2,j}^{th} = \left[1 + (\delta_1 + \beta_1 j^2)^2\right]^{1/2} (1 + \delta_2^2)^{1/2},\tag{10}$$

where $\eta_2 = 2\mu h_2/\gamma_1\gamma_2$ is the normalized pump amplitude. The same threshold equation can be obtained using a more general approach; namely, one can set $F_j, F_{-j}^* \propto \exp(-i\nu t)$ to determine the complex characteristic exponent $\nu = \nu' + i\nu''$ via a linear stability analysis. Then, one can make sure that $\nu'' > 0$ for $\eta_2 > \eta_{2,j}^{th}$, while $\nu'' < 0$ for $\eta_2 < \eta_{2,j}^{th}$. Thus, small amplitudes $F_{\pm j}(t)$ decay below the threshold and grow exponentially above it. This fully justifies the use of the threshold Equation (10). Note that similar relations with different notations are known in the literature.

Consider in some detail the threshold properties given by Equation (10). Remarkably, it includes neither the walk-off parameter α nor the SH dispersion coefficient β_2. The threshold equation refers to the FH pairs j and $-j$. The value of j can be an integer or semi-integer depending on the type of solution in question. The thresholds are generally different for different $|j|$. However, the minimal in δ_1 values of η_2^{th} are the same for all $|j|$. The value of δ_1 minimizing the threshold for a pair $\pm j$ is $\delta_1^{(j)} = -\beta_1 j^2$; it is substantially different for different j^2. Using this property, one can excite selectively any $j, -j$ pair on demand. The absolute threshold minimum, $[\eta_2^{th}]_{min} = 1$, can be achieved indeed at $\delta_2 = 0$, i.e., at the exact resonant excitation of the pumped SH mode. It is clear now that the parameter η_2 can be expressed by the pump power as $\eta_2 = (\mathcal{P}/\mathcal{P}_{min}^{th})^{1/2}$.

Now we turn to the FH pumping scheme. It is relevant not only to the comb generation issue, but also to the SH excitation. This scheme is complex compared to the previous one for fairly simple reasons. The parametric instability requires sufficiently large values of the SH amplitude $S_0 = \bar{S}$. They can be achieved, in turn, only for sufficiently large values of the amplitude of the pumped mode $F_0 = \bar{F}(h_1)$. Keeping this fact in mind, we consider what happens if we admit the presence of small perturbations $\delta F(\varphi, t)$ and $\delta S(\varphi, t)$, such that $F = \bar{F} + \delta F$ and $S = \bar{S} + \delta S$. Substituting these expressions into Equation (8) with $h_2 = 0$, we see that the SH perturbation δS becomes linearly linked to the FH perturbation via the term $\bar{F}\delta F$, which was absent earlier. As a result, we must deal with a quartet of

perturbations F_j, F_{-j}^*, S_j, $S_{-j}^* \propto \exp(-i\nu t)$ instead of the former parametric pair F_j, F_{-j}^*. The characteristic equation for ν becomes a cumbersome four-degree algebraic equation including all linear parameters $\delta_{1,2}$, $\beta_{1,2}$, and α [54]. The threshold properties become complicated, and they cannot be covered by simple relations similar to Equation (10).

Nevertheless, a general overview and illustrations of the threshold properties, which do not pretend to be complete, are possible. We introduce first the normalized pump amplitude $\eta_1 = \sqrt{2}\mu h_1 / \gamma_1 \sqrt{\gamma_1 \gamma_2}$; this normalization is different from that relevant to the SH pumping. The presence of parameter α, ranging from 0 to very large values, in the threshold equation raises questions about the effect of walk off. It turns out that the lowest threshold value of η_1 at a zero walk off ($\alpha = 0$) corresponds to $j = 0$, i.e., to an internal instability of the dual background [54]. For detunings $\delta_{1,2} = 0$, this value is minimal, $\eta_{1,0}^{\text{th}} = 3\sqrt{2}$. With increasing $|\alpha|$, some quartets with $j \neq 0$ quickly become the easiest to excite. However, the optimal values of $|j|$ depend significantly on the dispersion coefficients. This is illustrated by Figure 6, which was obtained with the use of numerical methods.
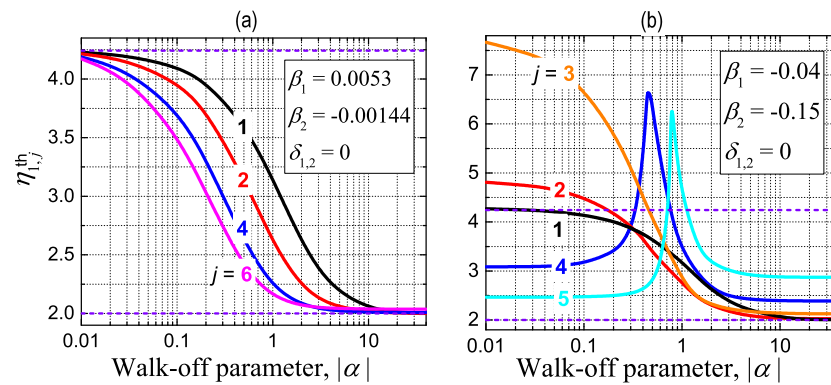

Figure 6. The threshold dependences $\eta_{1,j}^{\text{th}}(|\alpha|)$ for FH pumping at $\delta_{1,2} = 0$. (**a**) $\lambda_p \simeq 2698$ nm, $\beta_1 = 5.3$, and $\beta_2 = -1.44$ of 10^{-3}. (**b**) $\lambda_p \simeq 1664$ nm, $\beta_1 = -4$, $\beta_2 = -15$ of 10^{-2}. Two horizontal lines $3\sqrt{2} \simeq 4.24$ and 2 indicate the internal instability threshold and the limiting value $\eta_{1,j}^{\text{th}}(\infty) = 2$.

Figure 6a is plotted for $\delta_{1,2} = 0$ and the representative dispersion parameters relevant to the quasi-PM in LN. Within a broad range of $|\alpha|$, the lowest threshold corresponds to harmonics with very large values of $|j|$. Figure 6b corresponds to the natural PM, where the dispersion coefficients $\beta_{1,2}$ are negative and relatively large in their absolute values. The effect of $|\alpha|$ is strongly different here, and it strongly depends on $|j|$. The reason is in the competition between the walk off and dispersion terms entering the rate coefficient $Z_{2,l}$ given by Equation (5). Anyhow, the selective excitation of modes with $|j| = 1, 2$ is practically impossible. The effects of nonzero detunings of $\delta_{1,2}$ can also be investigated numerically. They also do not facilitate the selective excitation of harmonics with small values of $|j|$.

With increasing $|\alpha|$, the threshold values $\eta_{1,j}^{\text{th}}(\alpha)$ slowly approach two from above. This range is, however, not favorable for the soliton–comb generation because of a strong suppression of the side SH harmonics with $l \neq 0$, see also Sections 5 and 6.

4. Numerical Methods

We simulated predominantly set (3) in the coordinate frame moving with velocity v_1 by using the conventional fourth-order Runge–Kutta method [57]. Initially, for verification purposes, we also solved set (8) of the partial differential equations by using the step-split Fourier method [58]. The results were practically equivalent. The number of Fourier harmonics taken into account (and the mesh points in φ) ranged from 32 to 1024 within each of the FH and SH frequency domains. The accuracy of the calculations was controlled by changing the time step and number of harmonics. Different values of the variable input dimensionless parameters of the system ($\eta_{1,2}, \delta_{1,2}, \beta_{1,2}, \alpha$) were used. With harmonics $F_j(t), S_l(t)$ calculated, one can investigate the temporal evolution of the spatial

profiles $F(\varphi), S(\varphi)$ and comb spectra $|F_j|^2, |S_l|^2$. Additionally, it is possible to verify the establishment of steady states moving with a constant velocity and, if applicable, determine this velocity v_0.

Three main problems were considered numerically:

– We numerically verified the analytical results relevant to the instability thresholds. To do so, we used initial conditions with very small random complex values of $F_j(0)$ and $S_l(0)$ to see the initial exponential growth or decay of $|F_j|(t)$ for different values of $\eta_{1,2}$. Coincidence of the analytical and numerical results with a high accuracy was always achieved.

– We verified the stability of the dual soliton solutions obtained analytically in [52,56] for the known limiting cases. As the initial conditions, we used Fourier transforms of the relevant analytical expressions for $F(\varphi)$ and $S(\varphi)$. Numerical analyses has shown that all the analytical solutions are unstable: Temporal evolution inevitably leads to irregular spatial profiles and comb spectra.

– We tried to generate stable steady-state soliton–comb solutions starting from very small random complex amplitudes $F_j(0)$ and $S_l(0)$. As a rule, the evolution of our nonlinear systems well above the threshold ultimately leads to highly irregular saturated behavior after a stage of exponential growth. When abruptly switching the pump on, the rough features of this irregular behavior depend also on the choice of the initial conditions. Nevertheless, for many well-defined input parameters, proper pumping schemes, and not very abrupt switching the pump on, temporal evolution leads reliably and uniquely to multiparametric families of comb–soliton states. Below we describe the corresponding adiabatic procedure of growing soliton–comb states as applied (for definiteness) to the SH pumping case.

Let FH harmonics $\pm j$ possess the lowest threshold. For $\eta_2 < \eta_{2,j}^{\text{th}}$, we have then the steady state with $S_0 \neq 0$ and zero other harmonics. Switching to η_2 slightly above $\eta_{2,j}^{\text{th}}$, we obtain a steady state including S_0 and only a few relatively small other essential FH and SH harmonics. After that, the steady-state harmonics are used as new initial conditions at a slightly larger value of η_2. This procedure is repeated then many times to come to a steady state well above the threshold. The number of FH and SH harmonics taken into account has to be chosen properly. The final state is insensitive to the choice of the initial random amplitudes. The states achieved in this way can be qualified as self-starting steady states, and their stability is doubtless. Let us stress that the achievement of the soliton–comb states with the adiabatic procedure is not guaranteed. However, in many cases, it takes place.

The restriction on the rise time of the pump, τ_p, that is necessary to achieve the steady state is not very obligating. It is sufficient to fulfill the inequality $\gamma_{1,2}\tau_p \gg 1$, which corresponds typically to $\tau_p \gtrsim 1\,\mu$s. Note also that soliton–comb states can be achieved often in a few steps of step-wise increase in the pump power.

The establishment of soliton–comb steady states and the corresponding velocity v_0 can be quantified with a high accuracy by using a correlation method. We use the fact that the Fourier harmonic $A_j(t)$ (F_j or S_j) known in the coordinate frame moving with velocity v_1 can be recalculated in the frame moving with an arbitrary velocity v_* through multiplication by $\exp[ij(v_1 - v_*)t/R]$. Let us introduce the dimensionless error parameter

$$\varepsilon(t, \tau) = \frac{\sum_j |A_j(t) - A_j(t - \tau)|^2}{\sum_j (|A_j(t)|^2 + |A_j(t - \tau)|^2)}, \tag{11}$$

where A_j refers to a coordinate frame moving with velocity v_*, t is the calculation time, and τ is a variable time shift. Obviously, $\varepsilon(t, \tau)$ turns to zero only when we deal with the steady state and, simultaneously, $v_* = v$. The error parameter calculated for modestly large evolution times, $\gamma_{1,2}t \gtrsim 10^3$, and minimized over v_* shows extremely small values ($\varepsilon = 10^{-14}$–10^{-15}) caused by the numerical noise, see also below. For smaller t, i.e., during the transient stage, it is larger by many orders of magnitude. We thus have a numerical tool to control the establishment of steady states and to precisely determine the velocity v_0.

Figure 7 shows three examples of the temporal evolution of $\varepsilon(t, \tau)$ relevant to our adiabatic procedure applied to the antiperiodic case at $\gamma_{1,2} = \gamma = 10^7 \ \text{s}^{-1}$ and $\tau = 1/\gamma$; the parameters $\beta_1 = 0.02$, $\beta_2 = -0.01$, $\alpha = 1$ are representative for a close vicinity of the zero walk-off point in the LN-based resonators. The harmonics in question are F_j. The normalized pump amplitude η_2 sequentially takes 17 values above the threshold: 1.01, 1.1, ..., and 30. Figure 7 exhibits the evolution of ε after taking the first two and the last values at t_0, t_1, and t_{17}. The most general feature of this evolution is always the same: it is an almost exponential decrease in ε from initial values of the order of 1 to extremely low values of 10^{-14}–10^{-15}. Note also some quantitative details: The longest evolution, shown in Figure 7a, starts from modal noise. It takes about $(5$–$7)\gamma^{-1}$ for the harmonics to grow exponentially and reach the saturation. The corresponding evolution time can be identified with the rise time of the near-threshold optical parametric oscillation. The further evolution runs, which start from regular distributions of the FH and SH harmonics achieved during the previous runs, occur substantially faster. Our choice of taking 17 steps of evolution to reach the state with $\eta = 30$ is largely arbitrary. In many cases, the same final state can be achieved in a few steps.
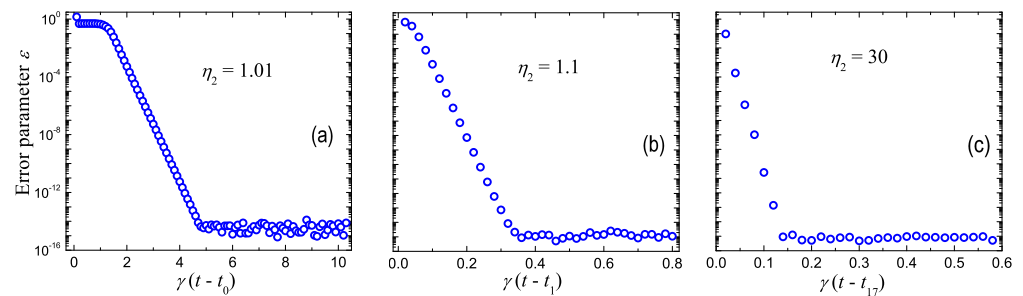

Figure 7. Three representative evolution runs for the error parameter $\varepsilon(t, \tau)$ relevant to the FH harmonics F_j and $\gamma\tau = 1$. The states under study are antiperiodic. The input dimensionless parameters are $\delta_{1,2} = 0$, $\beta_1 = 0.02$, $\beta_2 = -0.01$, $\gamma = 10^7 \ \text{s}^{-1}$, and $\alpha = 1$. The time step is $0.02\gamma^{-1}$. The evolution run relevant to (**a**) starts at t_0 from noise and ends up at t_1. The evolution runs (**b**,**c**) start from the previous steady-state values of the FH amplitudes.

In the next sections, we will see in detail the spatial and spectral properties of the dual states grown with the use of our adiabatic procedure.

5. Soliton–Comb States for SH Pumping

Below we report the results on soliton–comb generation obtained by using our adiabatic procedure in the SH pumping case for LN resonators [53,59]. The φ-dependences of $|F|^2$, $|S|^2$, $\arg[F]$, and $\arg[S]$ and the spectra $|F_j|^2$ and $|S_l|^2$ are of our prime interest. Additionally, we are interested in the dependences of the soliton–comb characteristics on the pump amplitude η_2, the walk-off parameter α, and other variable parameters of the system. Generally, the soliton position in the resonator depends on the choice of the initial random amplitudes. Since the azimuth angle φ can be counted from any point, we can chose its zero point as convenient.

We start our report with the case of quasi-PM via the radial poling. Here, the pump wavelength λ_p can take practically any value. In particular, it can be made arbitrary close to the zero walk-off point $\lambda_2^c \simeq 1349$ nm. This case is especially important. For sufficiently small values of $\delta\lambda = \lambda_p - \lambda_2^c$, the group velocity difference is given by $v_{12} \ [10^5 \ \text{cm/s}] \simeq -5.9 \times \delta\lambda \ [\text{nm}]$ in accordance with Figure 4a. Correspondingly, for $|\delta\lambda| \lesssim 10$ nm and typical values of R and γ_2, the walk-off parameter $\alpha = v_{12}/\gamma_2 R$ ranges from 0 to large negative and positive values, while the dispersion coefficients $\beta_{1,2}(\delta\lambda)$ stay practically constant and opposite in signs, $\beta_1 > 0$, $\beta_2 < 0$.

5.1. Antiperiodic Solutions Near $\lambda_2^c \simeq 1349$ nm

Figure 8 corresponds to an antiperiodic steady state moving with velocity $v_{01} = v_0 - v_1 = 0$. It is relevant to the zero walk off ($\delta\lambda = 0$, $\alpha = 0$); $\eta_2 = 30$; zero detunings ($\delta_{1,2} = 0$); $R = 1.5$ mm; and decay rates $\gamma_1 = 10^7$, $\gamma_2 = 10^8$ s^{-1} ($Q_1 \simeq 3.3 \times 10^7$, $Q_2 \simeq 0.7 \times 10^7$). The total number of harmonics taken into account is 1024. Figure 8a and Figure 8d show the central parts of the normalized FH and SH intensity profiles—the intensities stay constant far from the center. It is evident that we are dealing with a narrow dual dark–bright soliton. Far from the soliton core, the normalized values of $|F(\varphi)|^2$ and $|S(\varphi)|^2$ ($\simeq$29 and 1) nicely correspond to the dual background considered in Section 2. At the first sight, this feature is not consistent with the absence of the dual background for the antiperiodic states. The point is that the amplitude $F(\varphi)$ tends to the opposite left and right constant values far from the center, and these values can be found from Equation (8). The facts that (i) the intensity profiles are even in φ and (ii) the FH intensity $|F(\varphi)|^2$ turns exactly to zero at the soliton center are exclusively due to our zero walk-off assumption.
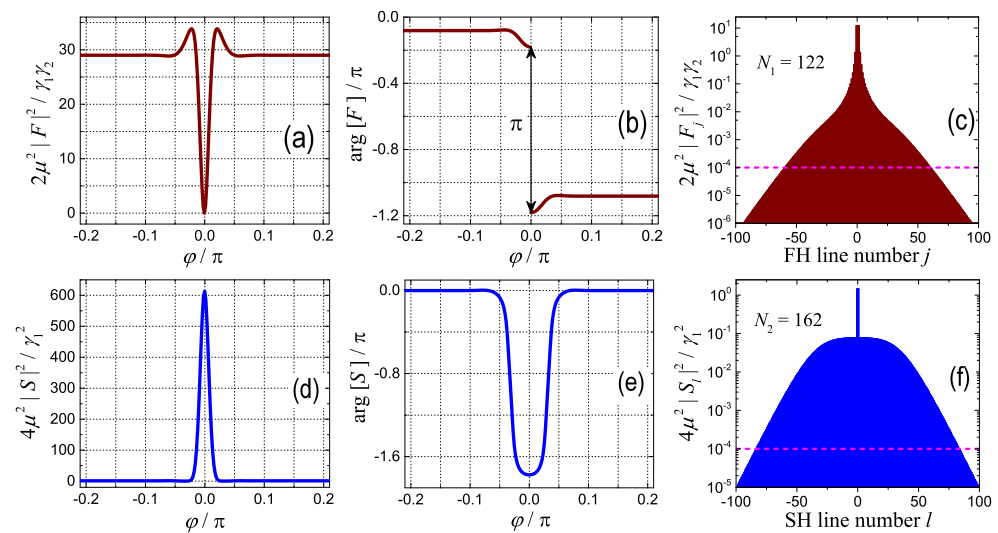

Figure 8. The properties of the antiperiodic steady state grown adiabatically for $\eta_2 = 30$, $R = 1.5$ mm, $\alpha = 0$, $\delta_{1,2} = 0$, $\beta_1 \simeq 0.02$, and $\beta_2 \simeq -0.01$; 1024 FH and SH harmonics are taken into account. The upper and lower rows refer to the FH and SH characteristics, respectively. They show the normalized intensity profiles (**a**,**d**), the phase profiles (**b**,**e**), and the comb spectra (**c**,**f**). The horizontal dashed lines indicate the cut-off level of 10^{-4}. The number of FH and SH comb lines above 10^{-4} is 122 and 162.

Figure 8b and Figure 8e exhibit φ-dependences of the phases $\arg[F]$ and $\arg[S]$. While an overall π change in $\arg[F]$ across the resonator is general for the antiperiodic states, the π jump at $\varphi = 0$ is typical only for $\alpha = 0$. More specifically, the line $\mathrm{Re}[F](\varphi), \mathrm{Im}[F](\varphi)$ on the complex plane crosses the zero point at a finite angle because of the symmetry leading to an abrupt π jump of the phase. For $\alpha \neq 0$, the function $\arg[F](\varphi)$ is smooth. Regarding the SH phase $\arg[S]$, only smooth (but large) deviations from zero are present near the soliton center, see Figure 8e.

The FH and SH comb spectra are shown in Figure 8c and Figure 8f. They are symmetric in j and l and very broad. The normalizations of F and S are slightly different and specific for the SH pumping case. On the other hand, they provide the maximum values of $|F_j|$ and $|S_l|$ of the order of one. The shapes of the FH and SH spectra are notably different. The central peak in Figure 8f is due to the pump. To quantify the comb spectra, we define the number of significant FH and SH lines (N_1 and N_2) whose normalized intensities are above the cut-off level 10^{-4}. This characteristic is conditional and rather useful; the lines of this strength are typically well above the light noise. In our case, $N_1 = 122$ and $N_2 = 161$ correspond to the well developed dual combs.

With increasing η_2, the dual soliton is progressively narrowing and the comb spectra are getting broader. No deterioration of the soliton–comb states was seen up to the maximal investigated values $\eta_2^{\text{max}} \approx 10^2$. Despite an apparent simplicity of the soliton profiles at $\alpha = 0$, no analytical solutions for them is known so far.

It is not difficult to estimate the numbers of light quanta $|F_j|^2/\hbar$ and $|S_l|^2/\hbar$ in the FH and SH modes for the data of Figure 8c and Figure 8f. Using Equation (4) for μ and setting $\sigma_{\text{eff}} = 100\,\mu\text{m}^2$, we have found that they are roughly of the order of 10^6 for $|j| \sim |l| \sim 1$. Thus, we are deeply within the classical range. This is valid also for the subsequent illustrations. At the same time, far tails of the comb spectra can experience quantum effects.

Next, we consider the effects of a nonzero walk-off. Nonzero values of α influence neither the thresholds nor the outcome of the adiabatic procedure—the system still evolves to a single-soliton steady state. The most evident effects are (i) a nonzero soliton velocity, $v_{01} \neq 0$, and (ii) asymmetry of the soliton profiles and the comb spectra. The larger the $|\alpha|$, the stronger is the asymmetry. This is illustrated by Figure 9. Compared to Figure 8, we changed $\delta\lambda$ from 0 to -1.08 nm, which corresponds to $\alpha \simeq 0.05$. The asymmetry of the soliton profiles and comb spectra is already evident. Furthermore, the soliton profiles acquire pronounced tails. The value of $|F(\varphi)|^2_{\text{min}}$ is now far from zero, and $|S(\varphi)|^2_{\text{max}}$ is about two times smaller than earlier. At the same time, the background values of the FH and SH intensities are the same, and the total number of the comb lines $N = N_1 + N_2$ is even slightly larger than it was at $\alpha = 0$. Changing the sign of $\delta\lambda$ results in the mirror reflection of the graphs of Figure 9 about the central vertical line and in the changed sign of the soliton velocity v_{01}.
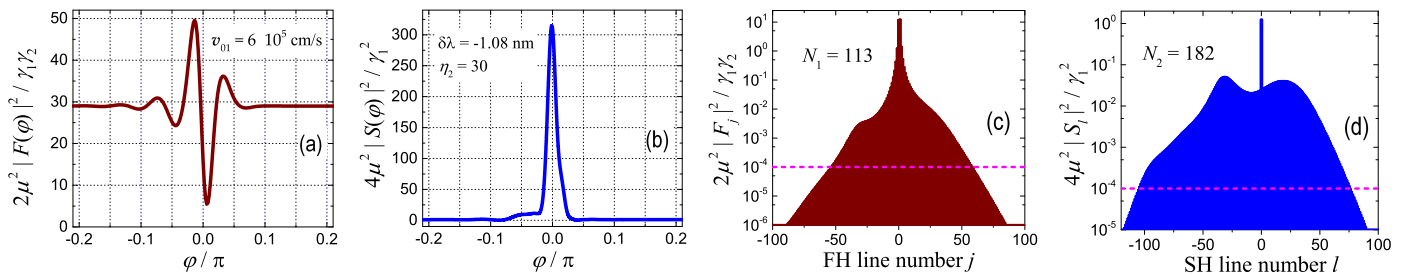

Figure 9. The effect of walk-off on the soliton–comb properties. The only difference in the input parameters as compared to Figure 8 is $\delta\lambda = \lambda_p - \lambda_2^c = -1.08$ nm corresponding to the walk-off parameter $\alpha \simeq 0.05$. The subfigures (**a**,**b**) show assimetry of the dual soliton intensiety profiles, while the subfigures (**c**,**d**) exhibit assimetry of the FH and SH comb spectra.

To gain new insights, we consider color maps of the velocity parameter $|v_{01}|/2\pi R$ and of the total comb line number $N = N_1 + N_2$ on the $\delta\lambda, \eta_2$ plane for a few representative combinations of the decay rates γ_1 and γ_2, see Figure 10. The first three subfigures of the upper row represent the maps of $|v_{01}|/2\pi R$ for the combinations $\gamma_{1,2} = \gamma$ (a1), $\gamma_1 = \gamma$, $\gamma_2 = 10\gamma$ (b1), and $\gamma_{1,2} = 10\gamma$ (c1) with $\gamma = 10^7\,\text{s}^{-1}$. Figure 10(a2,b2,c2) of the lower row represent the corresponding maps of the total comb line number N. Figure 10(d1,d2) give the additional cross-sections $v_{01}(\delta\lambda)$ and $N(\delta\lambda)$ at $\eta_2 = 20$ for our combinations of γ_1 and γ_2.

As evident from the maps, both $|v_{01}|$ and N grow monotonously with an increasing η_2. Regarding the dependences of these parameters on $|\delta\lambda|$ (or $|\alpha|$), they are decreasing only outside a vertical central strip, whose width depends on $\gamma_{1,2}$. The decrease of $N(|\delta\lambda|)$ and $|v_{01}|(|\delta\lambda|)$ persists for $|\delta\lambda| > 10$ nm. In short, large values of the walk-off parameter, $|\alpha| \gg 1$, are harmful for the soliton–comb generation in question.

The range of small $|\delta\lambda|$ (or α), illustrated in some detail in the Figure 10(d1,d2), is worthy of attention. The dependences $v_{01}(\delta\lambda)$ and $N(\delta\lambda)$ at large values of η_2 are not always continuous. This means that small variations in $\delta\lambda$ can lead to notably different results when adiabatically increasing η_2. Continuous changes in $v_{01}(\delta\lambda)$ and $N(\delta\lambda)$ at $\eta_2 = 20$ in Figure 10 take place only for $\gamma_1 = 0.1\gamma_2 = \gamma$. The optimum value of $|\delta\lambda|$ and

the corresponding largest peak values of N take place for $\gamma_{1,2} = 10\gamma$. In accordance with our definition of η_2, they correspond to the largest h_2 (and the pump power). Anyhow, the increase in N via the optimization of $\delta\lambda$ is not very large. Note lastly that the wavelength range of 20 nm relevant to Figure 10 strongly exceeds the intermodal wavelength distance of $\simeq 0.08$ nm so that the indicated spectral features are not available for the standard experimental fine-tuning means.
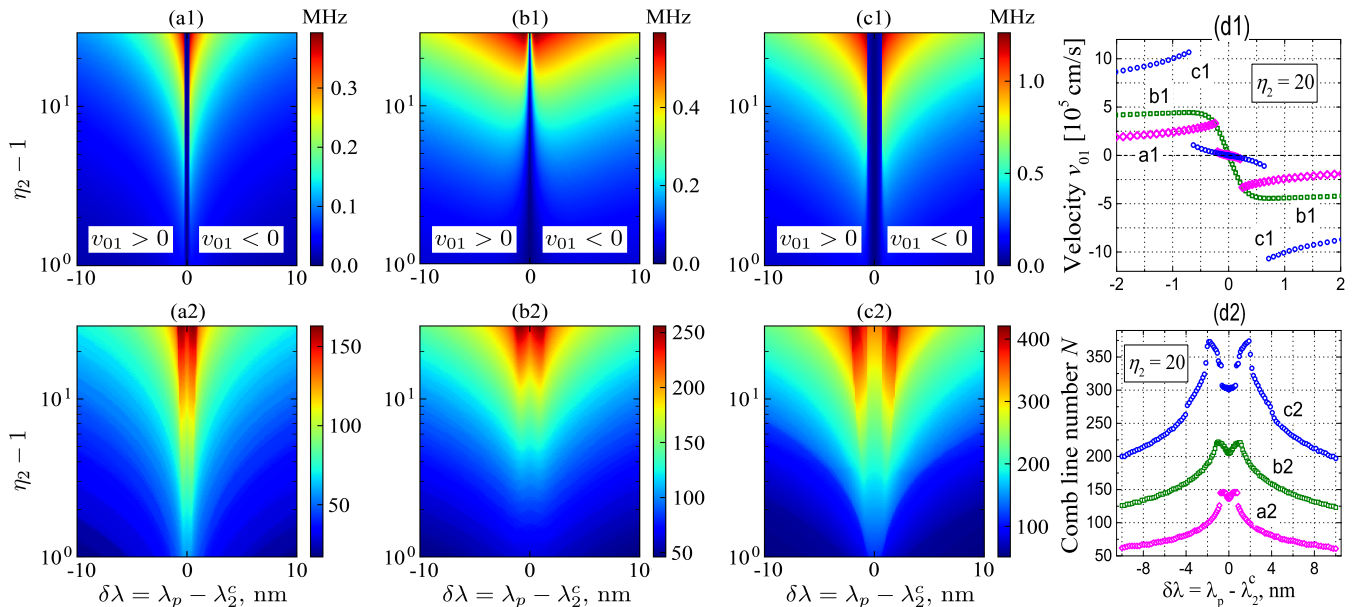
Figure 10. (**a1–c1**): Color maps of velocity parameter $|v_{01}|/2\pi R$ [MHz] on the $\delta\lambda, \eta_2$ plane. (**a2–c2**): The same for the total comb line number $N = N_1 + N_2$. The first, second, and third columns refer to $\gamma_{1,2} = \gamma$, $\gamma_1 = \gamma$, $\gamma_2 = 10\gamma$, and $\gamma_{1,2} = 10\gamma$ with $\gamma = 10^7$ s^{-1}. Each map is obtained by step-wise increase in η_2 starting from the value of 2 and incorporates the data of $141 \times 151 = 21291$ calculation variants with up to 1024 Fourier harmonics taken into account. The insets in a1 to c1 indicate the signs of v_{01}. (**d1,d2**) give the cross-sections $v_{01}(\delta\lambda)$ and $N(\delta\lambda)$ for $\eta = 20$ relevant to the maps (**a1–c1**) and (**a2–c2**), respectively. Note different scales of $\delta\lambda$ in (**d1,d2**).

Now we turn to the effects of the frequency detunings. These effects are of two kinds. One can consider the effects of $\delta_{1,2}$ on the initiation of soliton–comb states via an adiabatic increase in η_2. These strong and important effects are considered in Section 5.2. Alternatively, we can slowly vary $\delta_{1,2}$ upon reaching the above-considered soliton states at large values of η_2. This issue, which is largely (but not only) about the area of existence of the developed soliton–comb states, is considered below.

We have extended our adiabatic procedure for the slow independent changes in δ_1 and δ_2. In fact, two similar scanning procedures were used. Within the first one, we initially determined the soliton velocity v_{01} and the comb line number N by increasing and decreasing δ_1 at $\delta_2 = 0$. After that, starting from point $\delta_1, 0$, we increased and decreased the detuning δ_2. The achieved steady-state values of the amplitudes F_j and S_l were used as new initial conditions in each step of changing δ_1 or δ_2. Within the second procedure, the scanning order was inverted: initially, we varied δ_2 at $\delta_1 = 0$ and, after that, we increased and decreased δ_1 starting from points $0, \delta_2$. We have verified whether the functions $v_{01}(\delta_1, \delta_2)$ and $N(\delta_1, \delta_2)$ depend on the scanning order. Additionally, we have made sure that each steady state on the δ_1, δ_2 plane is still relevant to a single-soliton antiperiodic state.

Consider first the case of zero walk-off, $\alpha = 0$. In our coordinate frame moving with velocity v_1, the positive and negative propagation directions are equivalent, such that the soliton velocity difference $v_{01} = v_0 - v_1$ is expected to be zero. Surprisingly, we have found that this is not always the case. Figure 11a represents color map of $|v_{01}|/2\pi R$ for $\delta\lambda = 0$, $\gamma_1 = 10^7$, and $\gamma_2 = 10^8$ s^{-1} (as in Figure 8). The uniformly dark-blue-colored lower and

upper parts, which are separated from the rest by two slanted borders (bifurcation lines), correspond to $v_{01}/2\pi R = 0$ within an accuracy of $\sim 10^{-9}$ MHz. Between these borders we have a smooth distribution $|v_{01}|(\delta_1, \delta_2)$ whose scale is comparable with that of Figure 10. This distribution practically does not depend on the scanning order, so what is the sign of v_{01}? We have found that it randomly depends on the fine particularities of our calculation procedure, such as the presence of very weak remnant velocity perturbations. In essence, we have a clear example of the spontaneous symmetry breaking when the state with a high symmetry ($v_{01} = 0$) becomes unstable against the excitation of one of two equivalent states of lower symmetry with $|v_{01}| \neq 0$. One of the most known examples of such a symmetry breaking is the ferroelectric second-order transition below the Curie temperature.
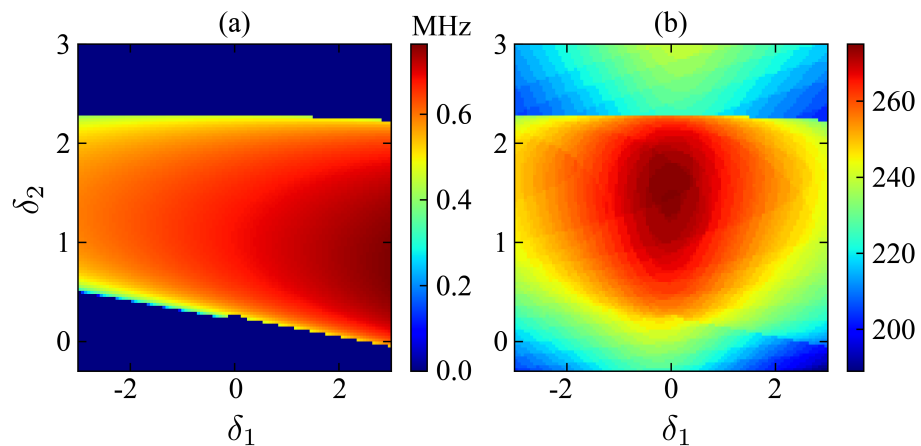

Figure 11. Dependences of $v_{01}/2\pi R$ (**a**) and N (**b**) on δ_1 and δ_2 for $\delta\lambda = 0$, $\gamma_1 = 10^7$, and $\gamma_2 = 10^8$ s^{-1}. Each map incorporates the data of $90 \times 90 = 8100$ calculation variants. Within the dark-blue-colored parts in (**a**), $v_{01} = 0$.

Let us now take a look at the corresponding color map of N, Figure 11b. The distribution $N(\delta_1, \delta_2)$ is rather smooth. The lower bifurcation line of Figure 11a is barely seen here, while the upper line is pronounced. Remarkably, the increase in δ_2 at $\delta_1 \approx 0$ is favorable for the comb in spite of the increasing instability threshold, see Equation (10). The characteristic scale in δ_1 here is about one, which strongly exceeds the scale $\beta_1 = 0.02$ relevant to the changes in $\eta_2^{\text{th}}(\delta_1)$. This assertion is general for $\eta_2 \gg 1$; it is justified by plotting maps of $N(\delta_1, \delta_2)$ for different values of $\delta\lambda$ and different combinations of γ_1 and γ_2. In short, we have a vast family of single-soliton antiperiodic states continuously depending on the input parameters.

Our attempts to generate periodic soliton–comb solutions at $\delta_{1,2} = 0$ failed. The reason why and the possibilities to obtain new solutions are indicated in Section 5.2.

5.2. Selective Generation of Periodic and Antiperiodic Multisoliton States

The idea for the generation of periodic and antiperiodic multisoliton states is rooted in the threshold conditions of Section 3 and a simple observation. The point is that the FH profile of Figure 8 with a sharp minimum emerges with increasing η_2 as a continuous (without bifurcations) development of the near-threshold profile $|F|^2 \propto \sin^2(\varphi/2)$ corresponding to the lowest threshold for FH harmonics with $j = \pm 1/2$. One can thus suggest that the spatial structure of developed solitons can be determined by the threshold conditions.

To develop this idea, we consider the excitation diagrams of Figure 12. Diagrams (a) and (b) correspond to the antiperiodic and periodic cases. The cyan circles on the horizontal δ_1/β_1 axis separate the regions where the lowest thresholds correspond to different values of the FH harmonic number $|j|$. Within a broad range in diagram (a), $\delta_1 > -\beta_1/2$, including the zero point, an adiabatic increase in η_2 is expected to lead to single-soliton antiperiodic states. This is in line with the above-considered results. For $-9\beta_1/4 < \delta_1 < -\beta_1/4$, we can expect three-soliton antiperiodic states, etc.

The periodic case, diagram (b), is expected to be different. In the range $\delta_1 > -\beta_1/2$, including the zero point, the lowest threshold corresponds to $j = 0$, i.e., to the generation of the dual background. As this background is stable, no periodic solitons are expected. However, in the range $-5\beta_1/2 < \delta_1 < -\beta_1/2$, where the lowest threshold corresponds to $|j| = 1$, a two-soliton periodic state is expected. Similarly, we can hope to generate four-soliton periodic states for $\delta_1 < -5\beta_1/2$. As concerned the detuning of δ_2, it plays a passive role by nonselectively increasing all thresholds according to Equation (10).
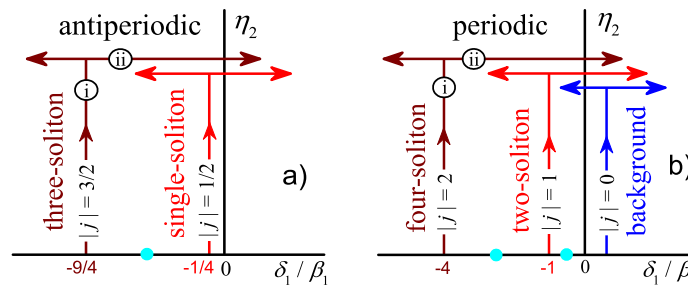
Figure 12. Diagrams of growth of antiperiodic (**a**) and periodic (**b**) multisoliton states by (i) adiabatic increase in η_2 and (ii) the subsequent slow change in δ_1. The cyan circles indicate the borders of the allowed ranges for initial values of δ_1/β_1. The lowest thresholds occur at $\delta_1^{(j)} = -\beta_1 j^2$. For $\eta_2 \gtrsim 10$, stable states grown via the adiabatic two-step (i–ii) procedure exist in a broad range of δ_1/β_1 exceeding the shown one.

Now we consider the results of the corresponding numerical experiments on the selective growth of multisoliton states [60]. Figure 13 shows the periodic two-soliton state grown via the adiabatic increase in η_2 for $\delta\lambda = 0$, $\gamma_{1,2} = \gamma = 10^7$ s^{-1}, $\delta_2 = 0$, and $\delta_1 = -\beta_1$. Remarkably, the phase $\arg[F](\varphi)$ shows two opposite π-steps when crossing each of the two narrow soliton areas. Thus, our periodic two-soliton solution consists of two equally spaced and mutually repelling antiperiodic solitons. This structure emerges every time spontaneously without imposing the antiperiodic conditions. The velocity of the state is $v_0 = v_1 = v_2$. The FH and SH comb spectra, shown in Figure 13c and Figure 13f, are symmetric and structurally similar to those of Figure 8c and Figure 8f. Because of the π-periodicity in φ, the comb line spacing is $2v_1/R$, and it is doubled compared to the single-soliton case. Correspondingly, the number of significant comb lines (above 10^{-4}) is about two times smaller than it would be in the single-soliton antiperiodic case at $\eta_2 = 20$. Remarkably, the spatial structures analogous (or similar) to those presented in Figure 13a,b,d,e were obtained independently in [61–63] for the periodic states and were interpreted as opposite domain walls.

Changing δ_1 sequentially to $\delta_1^{(j)} = -4\beta_1$ and $-9\beta_1$, which corresponds to the lowest threshold for $|j| = 2$ and 3, we have grown periodic four- and six-soliton states. They all consist of pairs of the same antiperiodic solitons. The comb line spacing increases with $|j|$ accordingly. A further increase in $|j|$ does not lead, however, to new multisoliton states. Temporal development tends to break such states into the former two-, four-, and six-soliton solutions. This feature is not related to an insufficiently small time step and/or an insufficiently large number of harmonics taken into account. Additionally, we mention the case $\delta_1 = 0$ relevant to the lowest threshold for $j = 0$. Our adiabatic procedure leads here, as expected, to a dual background steady state $\bar{F}, \bar{S}$.

Generalization of these results to the case of nonzero walk-off ($\alpha \neq 0$) and different decay rates γ_1 and γ_2 is rather trivial. We still have multisoliton periodic solutions consisting of pairs of the former antiperiodic solitons moving with velocity $v_0 \neq v_{1,2}$.
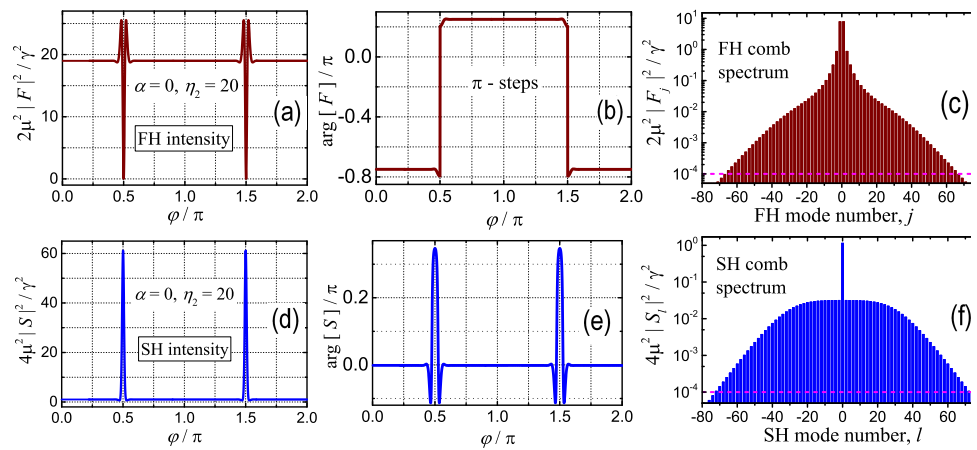
Figure 13. Periodic adiabatically grown two-soliton state for $\eta_2 = 20$, $\alpha = 0$, $\delta_1 = -\beta_1$, $\delta_2 = 0$, and $\gamma_{1,2} = \gamma = 10^7 \text{ s}^{-1}$. The upper and bottom rows refer to the FH and SH characteristics, respectively. They show the normalized intensity profiles (**a**,**d**), the phase profiles (**b**,**e**), and the comb spectra (**c**,**f**). An equal distance between the antiperiodic solitons indicates their mutual repulsion.

Now we switch to the multisoliton antiperiodic states relevant to semi-integer values of j, see Figure 12a. Figure 14 representatively shows the FH and SH intensity profiles for the antiperiodic three-soliton state grown for $\delta_1^{(3/2)} = -9\beta_1/4$ and $\alpha = -1$. The other input parameters are the same as in Figure 13. Each of the three equally spaced solitons has a familiar structure with oscillating tails. Owing to a relatively large negative value of α, the tails are strongly pronounced and the spatial asymmetry is inverted as compared to Figure 9. The soliton velocity difference is $v_{01} \simeq 2.2 \times 10^5$ cm/s. Interestingly, antiperiodic five- and seven-soliton states can be easily grown for $|j| = 5/2$ and $7/2$ in spite of the strong tail overlaps. This contrasts with the multisoliton periodic states.
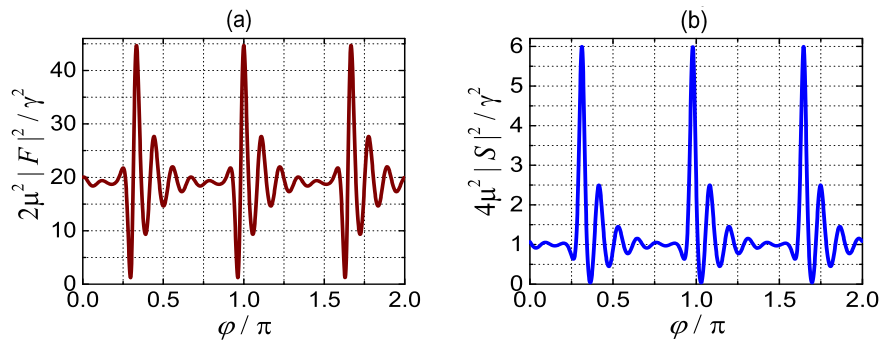

Figure 14. Antiperiodic adiabatically grown three-soliton state for $\alpha = -1$ ($\delta\lambda \simeq 8$ nm) and $\delta_1 = -9\beta_1/4$. The other parameters correspond to Figure 13. (**a**,**b**) correspond to the normalized FH and SH intensity profiles.

5.3. Natural PM: The Absence of Solitons

The natural phase matching that can be realized in LN-based resonators at $\lambda_2 \simeq 532$ nm is of special interest. Avoiding the complicated procedure of the radial poling and the availability of tunable laser sources in this range make it very attractive. Furthermore, it was indicated [64] that the value of the walk-off parameter can be substantially decreased for sufficiently small microresonators ($R < 1$ mm) by using the effects of geometric dispersion. This implies the use of proper Sellmeier equations for $n_{\text{o,e}}(\lambda)$ [32,65] and relations for the modal frequencies including the size corrections [29], see Section S2 of the Supplementary Materials for details. It turns out, however, that the main problem with the use of natural PM for the soliton–comb generation is the dispersion issue [66]. In contrast to the above-considered cases, the FH and SH dispersion parameters are both negative: $v'_1 \simeq -0.64$ and $v'_2 \simeq -1.5$ of 10^4 cm^2/s.

Aiming to see the role of the signs of the dispersion parameters, we first conducted some test numerical experiments. For $\gamma_{1,2} = 10^7 \text{ s}^{-1}$, $\alpha = 0$, $\delta_{1,2} = 0$, the absolute values $|\beta_1| = 0.02$ and $|\beta_2| = 0.01$, and four combinations of the signs of $\beta_{1,2}$, we have launched our adiabatic procedure to grow the antiperiodic soliton states. In two cases with $\beta_1 \beta_2 < 0$, we obtained the same known single-soliton solution, see Figure 8. In two other cases with $\beta_1 \beta_2 > 0$, we obtained no soliton states, and the comb spectra remained undeveloped. Additionally, we varied the values of the input parameters α, $\gamma_{1,2}$, and $\delta_{1,2}$ and switched from the antiperiodic to periodic case. No soliton solutions were found as well. The sign of the product $\beta_1 \beta_2$ is thus crucial for the soliton formation.

6. Solutions for FH Pumping

The case of FH pumping is important for experiment because it corresponds to the conditions of SH generation, including the tuning issues. At the first sight, switching to the FH pumping case is trivial—it is sufficient to set $h_2 = 0$ and $h_1 \neq 0$ in sets (3) and (8). The normalized pump amplitude is here $\eta_1 = \sqrt{2}\mu h_1 / \gamma_1 \sqrt{\gamma_1 \gamma_2}$, and only the periodic states are allowed. While the threshold conditions are more complicated now, they can be evaluated numerically for any set of the input parameters. With these preliminaries, we consider the most important cases [66].

We start from the vicinity of the zero walk-off point $2\lambda_c \simeq 2698$ nm. The value of the walk-off parameter α is controlled here by the wavelength difference $\delta\lambda = \lambda_p - 2\lambda_c$, and the dispersion coefficients $\beta_{1,2}$ can be treated as constants. Setting $\delta\lambda = 0$ ($\alpha = 0$) and $\delta_{1,2} = 0$ brings us to the situation where the lowest instability threshold, $\eta_1^{\text{th}} = 3\sqrt{2} \simeq 4.24$, corresponds to $j = 0$, i.e., to auto-oscillations of the dual background [54]. Figure 15 illustrates what happens with increasing η_1 when applying our adiabatic procedure at $\gamma_{1,2} = \gamma = 10^7 \text{ s}^{-1}$. We do see auto-oscillations of $|F_0|^2$ and $|S_0|^2$ near the threshold, see Figure 15a. The oscillation amplitude and period increases and decreases with increasing η_1, respectively, while the harmonics with $j, l \neq 0$ remain very small. For $\eta_1 \gtrsim 10$, these spatial harmonics become notable. Their amplitudes grow gradually, and the number of significant comb lines reaches $N \approx 10$ for $\eta_1 = 11$ with the comb line distance $\delta j = \delta l = 1$. The corresponding normalized FH and SH intensity profiles are shown in Figure 15b by lines 1 and 2. A further increase in η_1 results, however, in a sharp transition to an irregular spatial behavior, see Figure 15c and Figure 15d. This contrasts strongly with the case of SH pumping. Variations in the input parameters $\gamma_{1,2}$ and $\delta_{1,2}$ do not change this unfavorable scenario.
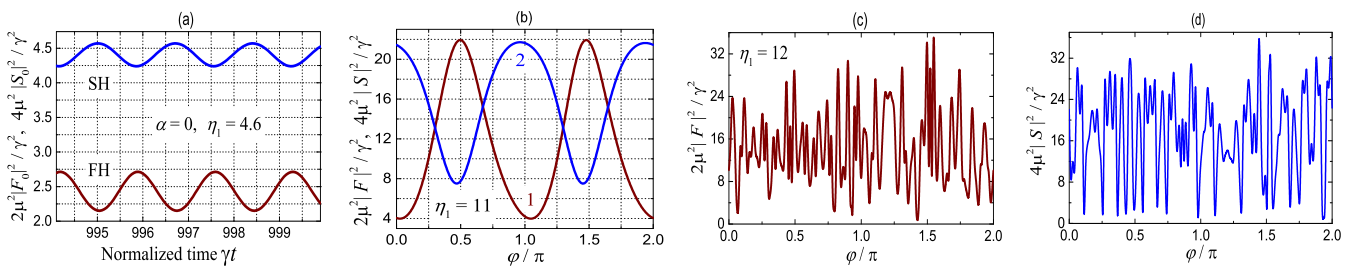

Figure 15. FH pumping at $\alpha = 0$ and $\delta_{1,2} = 0$. (**a**) A fragment of steady-state auto-oscillations at $\eta_1 = 4.6$; the spatial harmonics with $j, l \neq 0$ are negligible here. (**b**) FH and SH intensity profiles (lines 1 and 2) at $\eta_1 = 11$. (**c,d**) FH and SH intensity profiles at $\eta_1 = 12$.

With the increase in $|\alpha|$, the threshold values $\eta_{1,j}^{\text{th}}$ with $j \neq 0$ quickly decrease and become lower than the internal instability threshold. This is illustrated by Figure 6a relevant to our input parameters. For $\alpha \lesssim 1$, the modes with $|j| \gg 1$ possess the lowest thresholds. The application of our adiabatic procedure to the case $|\alpha| = 1$, $\delta_{1,2} = 0$ results, e.g., in the excitation of a $\pi/3$-periodic dual state (with six intensity peaks) near the threshold. With the increase in η_1, it transforms via a bifurcation to a $\pi/6$ periodic state (at $\eta_1 \simeq 6.7$). For $\eta_1 \gtrsim 16$, the system shows again an irregular spatial behavior. The number of significant

comb lines N does not exceed 25 for $\eta_1 \lesssim 16$. The employment of the nonzero detunings $\delta_{1,2}$ does not help much.

For $|\alpha| \gtrsim 10$, the threshold values $\eta_{1,j}^{\text{th}}(|\alpha|)$ approach two from above, and the selective excitation of harmonics with $|j| = |l| = 1, 2$ becomes possible. However, the thresholds for $|j| > 2$ are only slightly higher. Consider representatively the case $\alpha = 11$, $\delta_1 = 1/2$, and $\delta_2 = 0$ relevant to the lowest threshold for $|j, l| = 1$. Applying the adiabatic procedure, we have a π-periodic dual state near the threshold. For $\eta_1 \approx 7$ and 18, it transforms sequentially via bifurcations to $\pi/2$- and $\pi/4$-periodic states. Correspondingly, the comb line distance $\delta j = \delta l$ increases from 2 to 4 and lastly to 8. Figure 16a and Figure 16b show the complicated steady-state $\pi/4$-periodic asymmetric FH,SH intensity profiles for $\eta_1^{\text{max}} = 20$, while Figure 16c and Figure 16d exhibit the corresponding comb spectra. While the steady state found shows a regular spatial behavior, it cannot be regarded either as a soliton state or a pronounced comb state.
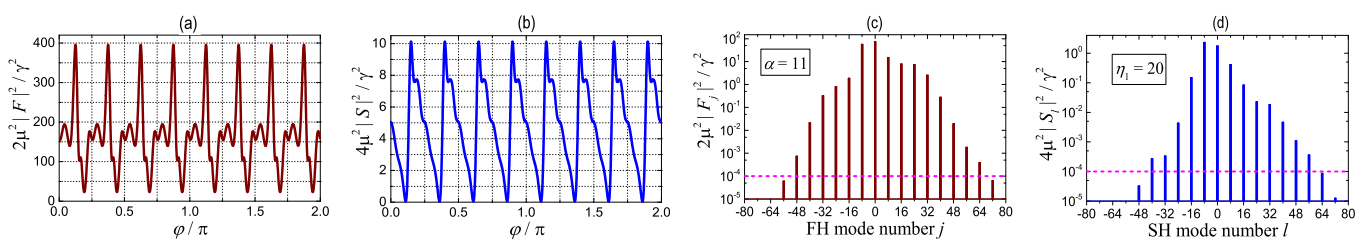

Figure 16. FH pumping at 2698 nm. (**a**,**b**) Periodic FH and SH intensity profiles for $\alpha = 11$, $\delta_1 = 1/2$, $\delta_2 = 0$, and $\eta_1 = 20$. (**c**,**d**) The corresponding FH and SH comb spectra. The number of significant comb lines (higher than 10^{-4}) is $N = 28$, and the comb line distance $\delta j = \delta l = 8$.

For $|\alpha| = 50$, the above scenario of the decreasing spatial period and increasing comb line distance with increasing η_1 remains the same. At $\eta_1 = 20$, we have a $\pi/3$ periodic dual state with a modest comb line number $N = 20$. The suppression of SH harmonics with $l \neq 0$ and the asymmetry of the intensity profiles and comb spectra are strongly pronounced.

Lastly, we touch on the case of the natural PM at $\lambda_p \simeq 1664$ nm, when small and/or modest values of $|\alpha|$ are available owing to the geometric dispersion, see Section S2 of the Supplementary Materials for details. The values of the quality factors $Q_{1,2}$ are expected to be substantially larger than they are at 2698 nm [67], which leads to larger absolute values of the dispersion coefficients $\beta_{1,2}$. As representative values, we chose $R = 1$ mm, $\beta_1 = -0.04$, and $\beta_2 = -0.15$, which corresponds to $Q_{1,2} \approx 3 \times 10^8$. The relevant dependences $\eta_{1,j}^{\text{th}}(\alpha)$ are presented in Figure 6b. While they differ from the threshold dependences of Figure 6a, one important feature is the same: it is impossible to selectively excite the modes with $|j| = 1, 2$ for $|\alpha| \lesssim 10$.

A large number of our numerical experiments, conducted with different values of α and modest absolute values of $\delta_{1,2}$, persistently show the same scenario: increasing η_1 above the threshold leads (via bifurcations) to dual states with smaller and smaller spatial periods (larger and larger comb line spacing) and, ultimately, to an irregular spatial behavior. The larger α, the longer is the interval of η_1 with the regular behavior. On the other hand, the number of significant comb lines N within this interval remains modest; it does not exceed 15. No signs of soliton–comb states were detected. Possibly, such states were seen in numerical calculations of [68,69] for sufficiently large mismatches.

7. Discussion

Experimental and theoretical studies of dissipative $\chi^{(2)}$ soliton–comb states in microresonators represent a vast, perspective, and almost unexplored research area. It is strongly different from the corresponding Kerr soliton research area. In turn, it is much broader than the studies of conservative Kerr solitons. The $\chi^{(2)}$ nonlinearity is fundamentally different from Kerr's one, which results in a number of specific qualitative features

including the duality of the nonlinear states and the necessity to employ the phase matching and minimize the temporal walk-off. The number of important variable parameters of the system is significantly larger than it is in the Kerr case. The deficit of analytical tools forces researches to rely on numerical methods.

Combining analytical and numerical tools and approaches, we predicted an unprecedentedly vast family of dual $\chi^{(2)}$ soliton–comb steady states. When using the term "vast", we mean a continuous dependence of the parameters of the state on all the input parameters—the pump power, the modal quality factors, the frequency detunings, and the walk-off. The found states are self-starting, i.e., they are easily accessible via not very abrupt switching the pump on and changing the detunings. The soliton–comb states are divided into two topological classes—periodic and antiperiodic—depending on the parity of the azimuth number of the pumped SH mode. The steady state solutions can be single- and multisoliton ones. All our soliton–comb states are dissipative; they cannot be reduced to (obtained from) the known conservative soliton solutions.

Remarkably, the predicted self-starting soliton–comb states are allowed only for the SH pumping. Furthermore, they require opposite signs of the FH and SH dispersion coefficients. This condition is fulfilled near the zero walk-off point $\lambda_2 \simeq 1349$ nm in LN-based resonators. However, the phase matching at this point requires a precise radial poling. Being available [15–18], it represents a serious technical problem. For natural phase matching in LN resonators, the necessary condition is not fulfilled, and soliton–comb states seem to be forbidden. Despite our strong efforts, no soliton–comb solutions were found for the FH pumping. This contradicts to the initial expectations about a similarity of the FH and SH pumping cases but has profound reasons behind it.

Both intuitive considerations and numerical modeling indicate that substantial differences in the FH-SH group velocities $v_{12} = v_1 - v_2$, which are typical of $\chi^{(2)}$ resonators, are unfavorable for soliton–comb generation. Quantitatively, this means that the combination $(|v_{12}|/c) \times (\lambda_2/R) \times Q_2$ has to be not much larger than one. This condition is not generally fulfilled for nonstructured high-Q resonators. The minimization of the walk-off parameter can be accomplished via a proper radial poling. Thus, there is one more physical reason to employ the radial poling for the $\chi^{(2)}$ comb generation.

Despite our massive failed efforts to find self-starting soliton–comb steady states for the FH pumping, we cannot claim that all sensible combinations of the input parameters (η_1, α, $\beta_{1,2}$, $\delta_{1,2}$, and $\gamma_{1,2}$) are exhausted. Additionally, we cannot claim that the initial assumption of the same transverse structure of the modes within each of the FH and SH frequency domains is fully justified. This problem still remains open for both the $\chi^{(2)}$ and $\chi^{(3)}$ resonators. It is likely that the suppression of the excitation of unwanted transverse modes requires further efforts for the mode management.

A distinctive feature of our approach is the employment of a simple classical equivalent of the Hamiltonian quantum formalism used in [4,5,17] and many other papers. While the quantum electrodynamic aspects of microresonators are important [17], the comb regimes belong to the classical range where the use of quantum language is redundant. As we have shown, the actual numbers of modal light quanta in the comb spectra are very large.

The effects of $\chi^{(3)}$ nonlinearity in $\chi^{(2)}$ microresonators is one more issue to consider. The possibility to neglect the $\chi^{(3)}$ nonlinearity is largely controlled by the modal Q factors. Let us consider for simplicity the SH pumping case. The pump power thresholds $\mathcal{P}_{\text{th}}^{(2)}$ and $\mathcal{P}_{\text{th}}^{(3)}$ for the parametric instability caused by the $\chi^{(2)}$ and $\chi^{(3)}$ nonlinearities are roughly proportional to $1/Q^3$ and $1/Q^2$, such that for $Q_{1,2} \gtrsim 10^6$, the effects of Kerr nonlinearity are expected to be negligible. For modest quality factors, $Q \lesssim 10^5$, which are typical, e.g., for ring waveguides, the situation can be more complicated. An interplay between the $\chi^{(2)}$ and $\chi^{(3)}$ nonlinear processes becomes possible [48].

The above-considered soliton–comb steady states in $\chi^{(2)}$ microresonators are not the first predicted ones and are known in the literature. To the best of our knowledge, the other known stable dissipative soliton states [46–49] belong to the periodic ones. Furthermore, they are not self-starting, i.e., not easily accessible. The single-soliton numerical solutions

of [46] are relevant to the FH pumping at the zero walk-off point. Both bright–bright and dark–dark locally stable solitons were exhibited. Similar numerical soliton solutions were found in [47,48]. Additionally, quasi-solitons at very large detunings, $|\delta_{1,2}| \gg 1$, were predicted. Remarkably, the soliton–comb states of [46] are allowed when the dispersion coefficients have the same and opposite signs. The generation of flat-top solitons via an additional spatial modulation of the pump amplitude was found numerically in the SH pumping case when the dispersion coefficients had opposite signs [49]. A considerable amount of soliton-related models, see, e.g., Ref. [70], were proposed for the bulk parametric oscillators. Their detailed analysis is beyond the scope of this mini-review.

The first experimental attempts to obtain $\chi^{(2)}$ combs in high-Q LN-based microresonators dealt with the FH pumping, the natural phase matching, and large walk-off [42,43]. Neither $\chi^{(2)}$ solitons nor broad comb spectra similar to the Kerr soliton spectra were observed. This is in agreement with our theoretical results on the necessary conditions for the realization of such regimes. The authors of [44] claim for the discovery the Pockels soliton microcomb in an aluminium nitride microring resonator by employing SH pumping. The parameters used correspond to modest quality factors $Q_{1,2} < 10^6$, a large walk-off parameter $|\alpha| \gg 1$, and the threshold power $\mathcal{P}_{th}^{(2)}$ only slightly below $\mathcal{P}_{th}^{(3)}$. The observed broad FH comb spectrum was practically symmetric, which is the fingerprint of the absence of the dominating contribution of the $\chi^{(2)}$ nonlinearity. The observed and numerically modeled combs are due to the Kerr nonlinearity. The quadratic nonlinearity is mostly involved in initiating the parametric instability, see also [71]. Thus, net $\chi^{(2)}$ soliton–comb states are still waiting for experimental discovery and exploration.

8. Conclusions

A vast family of stable soliton–comb steady states is accessible in $\chi^{(2)}$ microresonators by switching the monochromatic pump on not very abruptly. The necessary conditions for soliton–comb generation are (*i*) pumping into a SH resonator mode and (*ii*) the opposite signs of the FH and SH dispersion coefficients. Additionally, the minimization of the group velocity (free spectral range) difference for the phase-matched FH and SH modes is highly desirable. For LN-based resonators, the latter can be accomplished simultaneously with (*ii*) by using proper radial poling of the resonator. Pumping into FH resonator modes is not favorable for the realization of soliton–comb states. The employment of high-Q resonators ($Q > 10^7$) ensures low generation thresholds (within the μW range) and a negligibly small influence of the Kerr nonlinearity.

References

1. Del'Haye, P.; Schliesser, A.; Arcizet, O.; Wilken, T.; Holzwarth, R.; Kippenberg, T.J. Optical frequency comb generation from a monolithic microresonator. *Nature* **2007**, *450*, 1214–1217. [CrossRef]
2. Del'Haye, P.; Herr, T.; Gavartin, E.; Gorodetsky, M.L.; Holzwarth, R.; Kippenberg, T.J. Octave spanning tunable frequency comb from a microresonator. *Phys. Rev. Lett.* **2011**, *107*, 063901. [CrossRef] [PubMed]

3. Kippenberg, T.J.; Holzwarth, R.; Diddams, S.A. Microresonator-based optical frequency combs. *Science* **2011**, *332*, 555–559. [CrossRef] [PubMed]

4. Herr, T.; Brasch, V.; Jost, J.D.; Wang, C.Y.; Kondratiev, N.M.; Gorodetsky, M.L.; Kippenberg, T.J. Temporal solitons in optical microresonators. *Nat. Photonics* **2014**, *8*, 145–152. [CrossRef]

5. Kippenberg, T.J.; Gaeta, A.L.; Lipson, M.; Gorodetsky, M.L. Dissipative Kerr solitons in optical microresonators. *Science* **2018**, *361*, 567–572. [CrossRef]

6. Suh, M.G.; Vahala, K. Gigahertz-repetition-rate soliton microcombs. *Optica* **2018**, *5*, 65–66. [CrossRef]

7. Gaeta, A.L.; Lipson, M.; Kippenberg, T.J. Photonic-chip-based frequency combs. *Nat. Photonics* **2019**, *13*, 158–169. [CrossRef]

8. Chang, L.; Xie, W.; Shu, H.; Yang, Q.; Shen, B.; Boes, A.; Peters, J.D.; Jin, W.; Xiang, C.; Liu, S.; et al. Ultra-efficient frequency comb generation in AlGaAs-on-insulator microresonators. *Nat. Commun.* **2020**, *11*, 1331. [CrossRef]

9. Fujii, S.; Tanaka, S.; Ohtsuka, T.; Kogure, S.; Wada, K.; Kumazaki, H.; Tasaka, S.; Hashimoto, Y.; Kobayashi, Y.; Araki, T.; et al. Dissipative Kerr soliton microcombs for FEC-free optical communications over 100 channels. *Opt. Express* **2022**, *30*, 1351–1364. [CrossRef]

10. Fujii, S.; Wada, K.; Sugano, R.; Kumazaki, H.; Kogure, S.; Kato, Y.K.; Tanabe, T. Versatile tuning of Kerr soliton microcombs in crystalline microresonators. *Commun. Phys.* **2023**, *6*, 1–7. [CrossRef]

11. Akhmediev, N.; Ankiewicz, A. *Dissipative Solitons*; Lecture Notes in Physics; Springer: Berlin/Heidelberg, Germany, 2005.

12. Grelu, P.; Akhmediev, N. Dissipative solitons for mode-locked lasers. *Nat. Photonics* **2012**, *6*, 84–92. [CrossRef]

13. Boyd, R.W. *Nonlinear Optics*; Academic Press: New York, NY, USA, 2008.

14. Fürst, J.U.; Strekalov, D.V.; Elser, D.; Lassen, M.; Andersen, U.L.; Marquardt, C.; Leuchs, G. Naturally phase-matched second-harmonic generation in a whispering-gallery-mode resonator. *Phys. Rev. Lett.* **2010**, *104*, 153901. [CrossRef] [PubMed]

15. Beckmann, T.; Linnenbank, H.; Steigerwald, H.; Sturman, B.; Haertle, D.; Buse, K.; Breunig, I. Highly tunable low-threshold optical parametric oscillation in radially poled whispering gallery resonators. *Phys. Rev. Lett.* **2011**, *106*, 143903. [CrossRef]

16. Mohageg, M.; Strekalov, D.V.; Savchenkov, A.A.; Matsko, A.B.; Ilchenko, V.S.; Maleki, L. Calligraphic poling of lithium niobate. *Opt. Express* **2005**, *13*, 3408–3419. [CrossRef]

17. Strekalov, D.; Marquardt, C.; Matsko, A.B.; Schwefel, H.G.L.; Leuchs, G. Nonlinear and quantum optics with whispering gallery resonators. *J. Opt.* **2016**, *18*, 123002. [CrossRef]

18. Breunig, I. Three-wave mixing in whispering gallery resonators. *Laser Photonics Rev.* **2016**, *10*, 569–587. [CrossRef]

19. Buryak, A.V.; Di Trapani, P.; Skryabin, D.V.; Trillod, S. Optical solitons due to quadratic nonlinearities: From basic physics to futuristic applications. *Phys. Rep.* **2002**, *370*, 63–235. [CrossRef]

20. Ilchenko, V.S.; Savchenkov, A.A.; Matsko, A.B.; Maleki, L. Nonlinear optics and crystalline whispering gallery mode cavities. *Phys. Rev. Lett.* **2004**, *92*, 043903–043907. [CrossRef]

21. Jia, Y.; Hanka, K.; Zawilski, K.T.; Schunemann, P.G.; Buse, K.; Breunig, I. Continuous-wave whispering-gallery optical parametric oscillator based on $CdSiP_2$. *Opt. Express* **2018**, *26*, 10833–10841. [CrossRef]

22. Guo, X.; Zou, C.-L.; Tang, H.X. Second-harmonic generation in aluminum nitride microrings with 2500%/W conversion efficiency. *Optica* **2016**, *3*, 1126–1131. [CrossRef]

23. Kuo, P.S.; Bravo-Abad, J.; Solomon, G.S. Second-harmonic generation using $\bar{4}$-quasi-phasematching in a GaAs whispering-gallery-mode microcavity. *Nat. Commun.* **2013**, *5*, 3109. [CrossRef]

24. Gorodetsky, M.L. *High-Q Optical Microresonators*; Fizmatgiz: Moscow, Russia, 2011. (In Russian)

25. Matsko, A.B.; Ilchenko, V.S. Optical resonators with whispering-gallery modes—Part I: Basics. *IEEE J. Sel. Top. Quantum Electron.* **2006**, *12*, 3–14. [CrossRef]

26. Maleki, L.; Ilchenko, V.S.; Savchenkov, A.A.; Matsko, A.B. Crystalline whispering gallery mode resonators in optics and photonics. In *Practical Applications of Microresonators in Optics and Photonics*; Matsko A.B., Ed.; CRC Press: Boca Raton, FL, USA, 2019.

27. Gorodetsky, M.L.; Demchenko, Y.A. Accurate analytical estimates of eigenfrequencies and dispersion in whispering-gallery spheroidal resonators. *Proc. SPIE* **2012**, *8236*, 823623.

28. Demchenko, Y.A.; Gorodetsky, M.L. Analytical estimates of eigenfrequencies, dispersion, and field distribution in whispering gallery resonators. *J. Opt. Soc. Am. B* **2013**, *30*, 3056–3063. [CrossRef]

29. Breunig, I.; Sturman, B.; Sedlmeir, F.; Schwefel, H.G.L.; Buse, K. Whispering gallery modes at the rim of an axisymmetric optical resonator: Analytical versus numerical description and comparison with experiment. *Opt. Express* **2013**, *21*, 30683–30692. [CrossRef] [PubMed]

30. Sturman, B.; Podivilov, E.; Werner, C.S.; Breunig, I. Vectorial perturbation theory for axisymmetric whispering gallery resonators. *Phys. Rev. A* **2019**, *99*, 013810. [CrossRef]

31. Sturman, B.; Breunig, I. Generic description of second-order nonlinear phenomena in whispering-gallery resonators. *J. Opt. Soc. Am. B* **2011**, *28*, 2465–2471. [CrossRef]

32. Nikogosyan, D.N. *Nonlinear Optical Crystals: A Complete Survey*; Springer: New York, NY, USA, 2005.

33. Xiong, C.; Pernice, W.H.P.; Sun, X.; Schuck, C.; Fong, K.Y.; Tang, H.X. Aluminum nitride as a new material for chip-scale optomechanics and nonlinear optics. *New J. Phys.* **2012**, *14*, 095014. [CrossRef]

34. Werner, C.S.; Yoshiki, W.; Herr, S.J.; Breunig, I.; Buse, K. Geometric tuning: Spectroscopy using whispering-gallery resonator frequency-synthesizers. *Optica* **2017**, *4*, 1205–1208. [CrossRef]

35. Uvila, V.; Phillips, C.R.; Halonen, L.; Vainio, M. Frequency comb generation by a continuous-wavepumped optical parametric oscillator based on cascading quadratic nonlinearities. *Opt. Lett.* **2013**, *38*, 4281–4284. [CrossRef]

36. Uvila, V.; Phillips, C.R.; Halonen, L.; Vainio, M. High-power mid-infrared frequency comb from a continuous-wave-pumped bulk optical parametric oscillator. *Opt. Express* **2014**, *22*, 10535–10543. [CrossRef] [PubMed]

37. Ricciardi, I.; Mosca, S.; Parisi, M.; Maddaloni, P.; Santamaria, L.; De Natale, P.; De Rosa, M. Frequency comb generation in quadratic nonlinear media. *Phys. Rev. A* **2015**, *91*, 063839. [CrossRef]

38. Leo, F.; Hansson, T.; Ricciardi, I.; De Rosa, M.; Coen, S.; Wabnitz, S.; Erkintalo, M. Walk-off-induced modulation instability, temporal pattern formation, and frequency comb generation in cavity-enhanced second-harmonic generation. *Phys. Rev. Lett.* **2016**, *116*, 033901. [CrossRef]

39. Mosca, S.; Ricciardi, I.; Parisi, M.; Maddaloni, P.; Santamaria, L.; De Natale, P.; De Rosa, M. Direct generation of optical frequency combs in $\chi^{(2)}$ nonlinear cavities. *Nanophotonics* **2016**, *5*, 316–331. [CrossRef]

40. Mosca, S.; Parisi, M.; Ricciardi, I.; Leo, F.; Hansson, T.; Erkintalo, M.; Maddaloni, P.; De Natale, P.; Wabnitz, S.; De Rosa, M. Modulation instability induced frequency comb generation in a continuously pumped optical parametric oscillator. *Phys. Rev. Lett.* **2018**, *121*, 093903. [CrossRef]

41. Jankowski, M.; Marandi, A.; Phillips, C.R.; Hamerly, R.; Ingold, K.A.; Robert, L.; Byer, R.L.; Fejer, M.M. Temporal simultons in optical parametric oscillators. *Phys. Rev. Lett.* **2018**, *120*, 053904. [CrossRef] [PubMed]

42. Szabados, J.; Puzyrev, D.N.; Minet, Y.; Reis, L.; Buse, K.; Villois, A.; Skryabin, D.V.; Breunig, I. Frequency comb generation via cascaded second-order nonlinearities in microresonators. *Phys. Rev. Lett.* **2020**, *124*, 203902. [CrossRef]

43. Szabados, J.; Sturman, B.; Breunig, I. Frequency comb generation threshold via second-harmonic excitation in $\chi^{(2)}$ optical microresonators. *APL Photonics* **2020**, *5*, 116102. [CrossRef]

44. Bruch, A.W.; Liu, X.; Gong, Z.; Surya, J.B.; Li, M.; Zou, C.-L.; Tang, H.X. Pockels soliton microcomb. *Nat. Photonics* **2021**, *15*, 21–27. [CrossRef]

45. Liu, X.; Gong, Z.; Bruch, A.W.; Surya, J.B.; Lu, J.; Tang, H.X. Aluminum nitride nanophotonics for beyond-octave soliton microcomb generation and self-referencing. *Nat. Commun.* **2021**, *12*, 5428. [CrossRef]

46. Hannson, T.; Parra-Rivas, P.; Bernard, M.; Leo, F.; Gelens, L.; Wabnitz, S. Quadratic soliton combs in doubly resonant second-harmonic generation. *Opt. Lett.* **2018**, *43*, 6033–6036. [CrossRef] [PubMed]

47. Villois, A.; Skryabin, D. Soliton and quasi-soliton frequency combs due to second harmonic generation in microresonators. *Opt. Express* **2019**, *27*, 7098–7107. [CrossRef] [PubMed]

48. Villois, A.; Kondratiev, N.; Breunig, I.; Puzyrev, D.N.; Skryabin, D.V. Frequency combs in a microring optical parametric oscillator. *Opt. Lett.* **2019**, *44*, 4443–4446. [CrossRef] [PubMed]

49. Lobanov, V.E. Two-color flat-top solitons in microresonator-based optical parametric oscillators. *Phys. Rev. A* **2020**, *102*, 013518. [CrossRef]

50. Landau, L.D.; Lifshitz, E.M. *Mechanics*, 3rd ed.; Elsevier Ltd.: Amsterdam, The Netherlands, 1976.

51. Zakharov, V.E.; Kuznetsov, E.A. Hamiltonian formalism for nonlinear waves. *Phys. Uspekhi* **1997**, *40*, 1087–1116. [CrossRef]

52. Podivilov, E.; Smirnov, S.; Breunig, I.; Sturman, B. Nonlinear solutions for $\chi^{(2)}$ frequency combs in optical microresonators. *Phys. Rev. A* **2020**, *101*, 023815. [CrossRef]

53. Smirnov, S.; Sturman, B.; Podivilov, E.; Breunig, I. Walk-off controlled self-starting frequency combs in $\chi^{(2)}$ optical microresonators. *Opt. Express* **2020**, *28*, 18006–18017. [CrossRef]

54. Sturman, B.; Podivilov, E.; Szabados, J.; Breunig, I. Dual backgrounds and their stability during frequency comb and second harmonic generation in $\chi^{(2)}$ microresonators. *J. Opt. Soc. Am. B* **2022**, *39*, 378–387. [CrossRef]

55. Arnold, V.I.; Afrajmovich, V.S.; Il'yashenko, Y.S.; Shil'nikov, L.P. *Dynamical Systems V: Bifurcation Theory and Catastrophe Theory*; Springer: Berlin/Heidelberg, Germany, 1994.

56. Podivilov, E.; Sturman, B.; Breunig, I. Frequency comb solutions for driven $\chi^{(2)}$ optical microresonators. *J. Opt. Soc. Am. B* **2020**, *37*, 3316–3324. [CrossRef]

57. *Numerical Recipes 3rd Edition: The Art of Scientific Computing*; Cambridge University Press: New York, NY, USA, 2007; pp. 907–910.

58. Taha, T.R.; Ablowitz, M.I. Analytical and numerical aspects of certain nonlinear evolution equations. II. Numerical, nonlinear Schrödinger equation. *J. Comput. Phys.* **1984**, *22*, 203–230. [CrossRef]

59. Smirnov, S.; Andryushkov, V.; Podivilov, E.; Sturman, B.; Breunig, I. Soliton based $\chi^{(2)}$ combs in high-Q optical microresonators. *Opt. Express* **2021**, *29*, 27434–27449. [CrossRef] [PubMed]

60. Podivilov, E.; Smirnov, S.; Sturman, B. Adiabatic growing, multistability, and control of soliton-comb states in $\chi^{(2)}$ microresonators for pumping into second-harmonic modes. *JETP Lett.* **2022**, *115*, 553–559. [CrossRef]

61. Parra-Rivas, P.; Gelens, L.; Hansson, T.; Wabnitz, S.; Leo, F. Frequency comb generation through the locking of domain walls in doubly resonant dispersive optical parametric oscillators. *Opt. Lett.* **2019**, *44*, 2004–2007. [CrossRef] [PubMed]

62. Parra-Rivas, P.; Arabi, C.M.; Leo, F. Parametric localized patterns and breathers in dispersive quadratic cavities. *Phys. Rev. A* **2020**, *101*, 063817. [CrossRef]

63. Parra-Rivas, P.; Gelens, L.; Leo, F. Localized structures in dispersive and doubly resonant optical parametric oscillators. *Phys. Rev. E* **2019**, *100*, 032219. [CrossRef]

64. Breunig, I. (Freiburg University, Freiburg, Germany). Personal communication, 2020.

65. Umemura, N.; Matsuda, D. Thermo-optic dispersion formula for the ordinary wave in 5 mol % MgO doped LiNbO₃ and its application to temperature insensitive second-harmonic generation. *Opt. Commun.* **2016**, *367*, 167–173. [CrossRef]

66. Smirnov, S.; Podivilov, E.; Sturman, B. Effects of dispersion and pumping scheme on soliton-comb generation in $\chi^{(2)}$ microresonators. *J. Opt. Soc. Am. B* **2023**, *40*, 515–522. [CrossRef]

67. Leidinger, M.; Fieberg, S.; Waasem, N.; Kühnemann, F.; Buse, K.; Breunig, I. Comparative study on three highly sensitive absorption measurement techniques characterizing lithium niobate over its entire transparent spectral range. *Opt. Express* **2015**, *23*, 21690–21705. [CrossRef]

68. Arabi, C.M.; Parra-Rivas, P.; Hansson, T.; Gelens, L.; Wabnitz, S.; Leo, F. Localized structures formed through domain wall locking in cavity-enhanced second-harmonic generation. *Opt. Lett.* **2020**, *45*, 5856–5859. [CrossRef]

69. Parra-Rivas, P.; Arabi, C.M.; Leo, F. Dark quadratic localized states and collapsed snaking in doubly resonant dispersive cavity enhanced second-harmonic generation. *Phys. Rev. A* **2021**, *104*, 063502. [CrossRef]

70. Parra-Rivas, P.; Arabi, C.M.; Leo, F. Dissipative localized states and breathers in phase-mismatched singly resonant optical parametric oscillators: Bifurcation structure and stability. *Phys. Rev. Res.* **2022**, *4*, 013044. [CrossRef]

71. Englebert, N.; De Lucia, F.; Parra-Rivas, P.; Arabi, C.M.; Sazio, P.J.; Gorza, S.P.; Leo, F. Parametrically driven Kerr cavity solitons. *Nat. Photonics* **2021**, *15*, 857–861. [CrossRef]